

# The Giant Gemini GMOS survey of $z_{\text{em}} > 4.4$ quasars – I. Measuring the mean free path across cosmic time

Gábor Worseck,<sup>1,2\*</sup> J. Xavier Prochaska,<sup>1,2</sup> John M. O’Meara,<sup>3</sup> George D. Becker,<sup>4</sup>  
Sara L. Ellison,<sup>5</sup> Sebastian Lopez,<sup>6</sup> Avery Meiksin,<sup>7</sup> Brice Ménard,<sup>8,9,10</sup>  
Michael T. Murphy<sup>11</sup> and Michele Fumagalli<sup>12,13</sup>

<sup>1</sup>Max-Planck-Institut für Astronomie, Königstuhl 17, D-69117 Heidelberg, Germany

<sup>2</sup>Department of Astronomy and Astrophysics, UCO/Lick Observatory, University of California, 1156 High Street, Santa Cruz, CA 95064, USA

<sup>3</sup>Department of Chemistry and Physics, Saint Michael’s College, One Winooski Park, Colchester, VT 05439, USA

<sup>4</sup>Kavli Institute for Cosmology and Institute of Astronomy, Madingley Road, Cambridge CB3 0HA, UK

<sup>5</sup>Department of Physics and Astronomy, University of Victoria, Victoria, BC V8P 1A1, Canada

<sup>6</sup>Departamento de Astronomía, Universidad de Chile, Casilla 36-D, Santiago, Chile

<sup>7</sup>Scottish Universities Physics Alliance, Institute for Astronomy, University of Edinburgh, Blackford Hill, Edinburgh EH9 3HJ, UK

<sup>8</sup>Department of Physics & Astronomy, John Hopkins University, 3400 N. Charles Street, Baltimore, MD 21218, USA

<sup>9</sup>Kavli IPMU (WPI), The University of Tokyo, Kashiwa 277-8583, Japan

<sup>10</sup>Alfred P. Sloan Fellow

<sup>11</sup>Centre for Astrophysics and Supercomputing, Swinburne University of Technology, Hawthorn, Victoria 3122, Australia

<sup>12</sup>Department of Physics, Durham University, South Road, Durham DH1 3LE, UK

<sup>13</sup>Carnegie Observatories, 813 Santa Barbara Street, Pasadena, CA 91101, USA

Draft version 6 June 2018

## ABSTRACT

We have obtained spectra of 163 quasars at  $z_{\text{em}} > 4.4$  with the Gemini Multi Object Spectrometers on the Gemini North and South telescopes, the largest publicly available sample of high-quality, low-resolution spectra at these redshifts. From this homogeneous data set, we generated stacked quasar spectra in three redshift intervals at  $z \sim 5$ . We have modelled the flux below the rest-frame Lyman limit ( $\lambda_r < 912 \text{ \AA}$ ) to assess the mean free path  $\lambda_{\text{mfp}}^{912}$  of the intergalactic medium to H I-ionizing radiation. At mean redshifts  $z_q = 4.56, 4.86$  and  $5.16$ , we measure  $\lambda_{\text{mfp}}^{912} = (22.2 \pm 2.3, 15.1 \pm 1.8, 10.3 \pm 1.6) h_{70}^{-1}$  proper Mpc with uncertainties dominated by sample variance. Combining our results with  $\lambda_{\text{mfp}}^{912}$  measurements from lower redshifts, the data are well modelled by a simple power-law  $\lambda_{\text{mfp}}^{912} = A [(1+z)/5]^\eta$  with  $A = (37 \pm 2) h_{70}^{-1}$  Mpc and  $\eta = -5.4 \pm 0.4$  between  $z = 2.3$  and  $z = 5.5$ . This rapid evolution requires a physical mechanism – beyond cosmological expansion – which reduces the cosmic effective Lyman limit opacity. We speculate that the majority of H I Lyman limit opacity manifests in gas outside galactic dark matter haloes, tracing large-scale structures (e.g. filaments) whose average density (and consequently neutral fraction) decreases with cosmic time. Our measurements of the strongly redshift-dependent mean free path shortly after the completion of H I reionization serve as a valuable boundary condition for numerical models thereof. Having measured  $\lambda_{\text{mfp}}^{912} \approx 10 \text{ Mpc}$  at  $z = 5.2$ , we confirm that the intergalactic medium is highly ionized by that epoch and that the redshift evolution of the mean free path does not show a break that would indicate a recent end to H I reionization.

**Key words:** dark ages, reionization, first stars – diffuse radiation – galaxies: formation – intergalactic medium – quasars: absorption lines.

## 1 INTRODUCTION

The current cosmological paradigm posits that  $\approx 1$  Gyr after the Big Bang compact sources – stars, accreting black holes – gen-

erate sufficient ionizing radiation to reionize the neutral hydrogen throughout the bulk of the intergalactic medium (IGM). Indeed, the spectra of distant quasars and gamma-ray bursts reveal a forest of Ly  $\alpha$  absorption lines which are characteristic of a highly ionized medium at  $z \lesssim 6$  (e.g. Gunn & Peterson 1965; Chen et al. 2005). Resolving the epoch of reionization, its timing and the nature of

\* E-mail: gabor@mpia-hd.mpg.de

these ionizing sources stands as one of the outstanding challenges of modern cosmology.

While the community eagerly awaits results of low-frequency radio observations to probe the reionization epoch via the 21cm hyperfine transition (e.g. Zaroubi et al. 2012; Yatawatta et al. 2013; Pober et al. 2013; Beardsley et al. 2013), researchers have been studying effects of reionization on the IGM in absorption through spectroscopy of background sources. These include the most distant quasars (Fan et al. 2006; Mortlock et al. 2011) and  $z > 8$  gamma-ray bursts ‘revealed’ by their extremely faint optical fluxes (Kawai et al. 2006; Cucchiara et al. 2011; Chornock et al. 2013). Analysis of these data suggest the transition to a predominantly ionized universe occurs at  $z \gtrsim 6$  (White et al. 2003; Bolton et al. 2011), where a sharp increase in the effective Ly $\alpha$  opacity may occur (but see Becker, Rauch & Sargent (2007)).

Preferably, one would trace evolution in the ionization state of the IGM in the Lyman continuum which has an effective opacity nearly four orders of magnitude smaller than Ly $\alpha$  and is therefore far more sensitive to the neutral fraction of hydrogen. The effective Lyman Limit (LL) opacity is frequently represented by the mean free path  $\lambda_{\text{mfp}}^{912}$ , defined here to be the physical distance a packet of ionizing photons can travel before encountering an  $e^{-1}$  attenuation. By definition,  $\lambda_{\text{mfp}}^{912}$  approaches zero as one transitions into the reionization epoch (e.g. Gnedin 2000). After reionization, the mean free path is set by the distribution and evolution of residual neutral gas in the universe. This will include dense, collapsed structures (e.g. galaxies) but the opacity may be dominated by more diffuse gas in the outskirts of dark matter haloes (e.g. Fumagalli et al. 2011) and even more distant and diffuse structures in the IGM. By assessing the redshift evolution of  $\lambda_{\text{mfp}}^{912}$ , one constrains the nature of structures providing the universe’s LL opacity and, as importantly, its attenuation of the ionizing sources which generate the extragalactic UV background (Faucher-Giguère et al. 2009; Haardt & Madau 2012).

Many previous works have estimated  $\lambda_{\text{mfp}}^{912}$  by first evaluating the H I frequency distribution  $f(N_{\text{HI}})$  of IGM absorbers (and its redshift evolution;  $f(N_{\text{HI}}, z)$ ) and then convolving this distribution with the photoionization cross-section (e.g. Meiksin & Madau 1993). Varying  $f(N_{\text{HI}}, z)$  within the observational uncertainties, this indirect approach has yielded estimates of 40 to  $150h_{70}^{-1}$  Mpc (proper) at  $z \sim 3$  in a  $\Lambda$ CDM cosmology (Madau, Haardt & Rees 1999; Faucher-Giguère et al. 2008a; Meiksin & Madau 1993). This approach is affected by uncertainty in  $f(N_{\text{HI}}, z)$  from line blending and clustering of absorbers contributing to the LL opacity, at least at  $z \sim 2.5$  (Rudie et al. 2013; Prochaska et al. 2014). Recently, the mean free path has been *directly* evaluated through the analysis of stacked rest-frame quasar spectra: at  $z \approx 4$  using data taken by the Sloan Digital Sky Survey (SDSS; Abazajian et al. 2009) and at  $z \sim 2 - 3$  with space and ground-based programmes (Prochaska, Worseck & O’Meara 2009; O’Meara et al. 2013; Fumagalli et al. 2013b). These results show a monotonic increase in  $\lambda_{\text{mfp}}^{912}$  with decreasing redshift, ranging from  $\approx 30 h_{70}^{-1}$  Mpc at  $z = 4$  to over  $200 h_{70}^{-1}$  Mpc at  $z = 2.5$ .

For  $z > 4$ , the current constraints on  $\lambda_{\text{mfp}}^{912}$  are much poorer owing to the small sample of quasars observed at sufficient signal-to-noise (S/N) to assess the Lyman continuum opacity. Our own analysis of the SDSS data set terminated at  $z = 4.2$  (Prochaska, Worseck & O’Meara 2009), and the SDSS-III survey offers few new bright sources at these redshifts (Pâris et al. 2013). Songaila & Cowie (2010) surveyed 25 quasars for Lyman limit systems (LLSs) with medium resolution Keck spectroscopy and discovered 20 absorbers with  $\tau_{912}^{\text{LL}} \geq 1$  at  $z > 4$ , but sampled only 10

systems at  $z > 4.5$ . Combining their results with previous surveys (Storrie-Lombardi et al. 1994; Péroux et al. 2003), they measured the incidence of LLSs to  $z \sim 5$  and inferred a mean free path of  $50h_{70}^{-1}$  Mpc at  $z = 3.5$  assuming a power-law frequency distribution  $f(N_{\text{HI}}) \propto N_{\text{HI}}^{-\beta}$  with a relatively flat  $\beta = 1.3$ . Again,  $f(N_{\text{HI}}, z)$  is poorly constrained at  $z > 3.5$ , especially at column densities  $N_{\text{HI}} \approx 10^{17} \text{ cm}^{-2}$  implying a significant ( $\sim 30$  per cent) systematic uncertainty in  $\lambda_{\text{mfp}}^{912}$  estimates.

In 2010, our group began a multi-semester campaign with the Gemini Multi Object Spectrometers (GMOSs; Hook et al. 2004) on the twin Gemini 8 m telescopes, to survey approximately 150 quasars at  $z_{\text{em}} > 4.4$ , discovered primarily by SDSS. The primary goal of this Giant Gemini GMOS (GGG) survey is to precisely measure  $\lambda_{\text{mfp}}^{912}$  at  $z \sim 5$ ; this is the focus of this manuscript. The data also enable estimates of the average IGM Lyman series opacity, studies of high- $z$  quasar emission properties, and a search for high- $z$  high-column density absorbers. Those topics will be considered in future manuscripts. In the following, we adopt a flat  $\Lambda$ CDM cosmology with  $H_0 = 70h_{70} \text{ km s}^{-1} \text{ Mpc}^{-1}$ ,  $\Omega_{\text{m}} = 0.30$ , and  $\Omega_{\Lambda} = 0.70$ . Unless noted otherwise, all distances quoted in this paper are proper and corrected to the used cosmology.

## 2 SAMPLE SELECTION

The primary goal of the GGG survey is to extend measurements of the mean free path to ionizing radiation to  $z > 4.2$ . Our methodology follows the techniques developed in Prochaska, Worseck & O’Meara (2009) and O’Meara et al. (2013), which we briefly summarize: (i) generate stacked rest-frame spectra of a random sample of quasars with a narrow range of emission redshift  $z_{\text{em}}$ ; (ii) model the average flux at rest wavelengths  $\lambda_{\text{r}} < 912 \text{ \AA}$  with a standard quasar spectral energy distribution (SED), an evolving Lyman series opacity from the H I forest, and an opacity set by the cumulative LL absorption of the IGM; (iii) calculate the distance from  $z_{\text{em}}$  where the flux is attenuated by  $e^{-1}$  from LL absorption alone. Unlike previous approaches which relied on evaluations of the H I frequency distribution  $f(N_{\text{HI}}, z)$ , our approach offers a nearly direct estimation of  $\lambda_{\text{mfp}}^{912}$ . Generally, the uncertainty is driven by sample variance, and possible systematic errors are estimated below.

To perform the  $\lambda_{\text{mfp}}^{912}$  measurement, we require a quasar data set with the following characteristics: (i) well measured emission redshifts ( $\sigma_v < 1000 \text{ km s}^{-1}$ ); (ii) a large sample of sources ( $N \gtrsim 50$ ) at nearly the same  $z_{\text{em}}$ ; (iii) a homogeneous, spectral data set in resolution, wavelength coverage and data reduction processing; (iv) coverage of the emission-line free  $\lambda_{\text{r}} \approx 1450 \text{ \AA}$  spectral region to scale the spectra to one another; (v) quasar spectra without strong broad absorption line features; (vi) a relative spectral fluxing accurate to a few per cent; (vii) a S/N per pixel in excess of  $\approx 5 \text{ \AA}^{-1}$  to minimize systematic error associated with continuum placement (for other projects) and sky subtraction.

Upon publication of Prochaska, Worseck & O’Meara (2009), we recognized that no such data set existed at  $z > 4$ . While the SDSS had discovered and observed several hundreds of quasars at those redshifts, the majority of these data had too low S/N for precise  $z_{\text{em}}$  measurements and may well suffer from systematic errors (e.g. poor sky subtraction) that preclude the generation of robust stacked spectra. Therefore, we initiated a programme on the Gemini North and South telescopes with the Gemini Multi Object Spectrometers (GMOSs; Hook et al. 2004) to observe over 150 quasars at  $z_{\text{em}} > 4.4$ . Details on the instrument configuration are presented

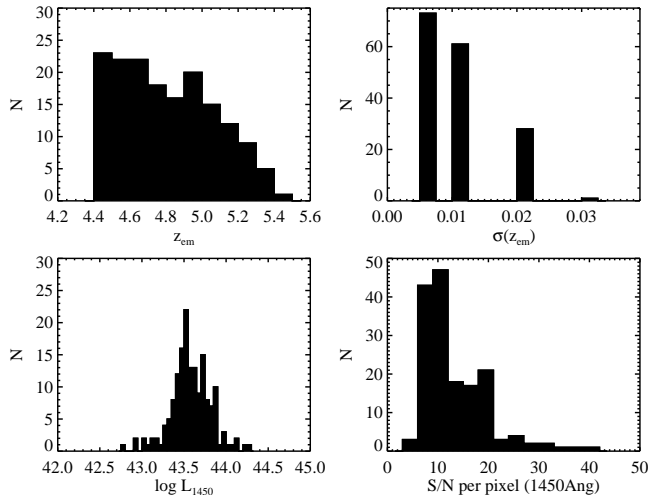


**Figure 1.** Histograms summarizing properties of the quasars and their spectra from the GGG survey (*top left*: quasar redshift; *top right*: estimated redshift error; *bottom left*: specific luminosity at rest-frame wavelength  $\lambda_r = 1450 \text{ \AA}$ ; *bottom right*: S/N per pixel at  $\lambda_r = 1450 \text{ \AA}$ ). The sample is restricted to quasars with  $z_{\text{em}} > 4.4$  and, given the magnitude limit of SDSS, comprise a very luminous cohort ( $L_{1450} \gtrsim 10^{43} \text{ erg s}^{-1} \text{ \AA}^{-1}$ ).

in the following section. At these high redshifts, the IGM strongly absorbs the quasar flux at wavelengths  $\lambda < 6500 \text{ \AA}$ . This implies that the colour selection algorithms used by SDSS to target these quasars are essentially free from any bias from the presence of LL absorption (Worseck & Prochaska 2011). In this respect, we consider the sample to be unbiased.

All of our targets were taken from the SDSS Data Release 7 (Abazajian et al. 2009). We began by retrieving the ‘best’ 1D spectrum for every source flagged as a  $z > 4.4$  quasar by the SDSS automatic redshift assignment routine, and proceeded to vet each of them through visual inspection of the SDSS spectra. We culled sources with apparent broad absorption line (BAL) features and those where  $z_{\text{em}}$  had been erroneously assigned. This provided a pool of  $\approx 380$  sources. From these we selected 163 for observations with Gemini. The precise target list represents a compromise between sampling the redshift interval  $z_{\text{em}} = [4.4, 5.5]$ , selecting sources sufficiently bright for an approximately one hour Gemini/GMOS observation, considerations on the number of sources per observing semester, maximizing the number of sources for Gemini South, and the availability of suitable guide stars. We believe that none of these criteria has an important impact on the LL absorption along the sight lines. Table A1 lists all of the sources observed in our programme. A visual summary of the main properties of our survey is provided in Fig. 1.

The only other survey of competitive size and quality at these redshifts is the sample developed by Songaila & Cowie (2010). Those authors observed 25 quasars at  $z_{\text{em}} > 4.17$  with Keck/ESI at high spectral resolution ( $R \sim 5300$ ) and S/N, and combined their sample with the literature (Péroux et al. 2003). However, this combined sample of 39  $z_{\text{em}} > 4.4$  quasars yields a rough  $\lambda_{\text{mfp}}^{0.12}$  estimate at best, owing to sample variance and the broad emission redshift distribution. As we will show below,  $\gtrsim 40$  sight lines per  $\Delta z \simeq 0.3$  are needed to track the redshift evolution of the mean free path at  $z > 4$ .

**Table 1.** Summary of our programme allocations.

Programme ID	Allocation [h]	Band	Observed QSOs
GN-2010A-Q-33	40	2	40
GS-2010A-Q-1	18	1	18
GN-2010B-Q-71	24	2	21
GS-2010B-Q-28	20	1	20
GN-2011A-Q-1	33	1	35
GS-2011A-Q-1	27	1	29

### 3 OBSERVATIONS AND DATA REDUCTION

We proposed for Gemini observing time through all partners in Semesters 2010A, 2010B, and 2011A. Altogether, we were allocated 162 hours for observations in queue mode, with 60 per cent allocated on Gemini North to efficiently cover the SDSS footprint. A summary of our programme is given in Table 1.

For every source, we obtained a spectrum through the  $1''$  longslit with two of the GMOS gratings: (i) the B600 grating blazed at  $4610 \text{ \AA}$  with a FWHM resolution of  $\approx 320 \text{ km s}^{-1}$  and an unbinned spectral dispersion of  $0.46 \text{ \AA pixel}^{-1}$  and; (ii) the R400 grating blazed at  $7640 \text{ \AA}$  with FWHM  $\approx 360 \text{ km s}^{-1}$  and a dispersion of  $0.69 \text{ \AA pixel}^{-1}$ . We binned the CCDs twice in the spatial dimension and 4 times spectrally, resulting in a sampling of  $\sim 3$  pixels per spectral resolution element. During our observing campaign both GMOSs were equipped with their original EEV 3 CCD mosaics. For every target we acquired two 900 s exposures with the B600 grating and a single 480 s exposure with the R400 grating. The exposures were taken together in an approximately 1 h continuous block including overheads for target acquisition, read-out and attached flatfield exposures. We dithered by  $50 \text{ \AA}$  between the B600 exposures to cover the spectral gaps between the 3-CCD mosaic of GMOS. The B600 grating tilt was set to cover down to a rest-wavelength of  $\approx 850 \text{ \AA}$  and therefore depended on the quasar’s emission redshift. The R400 grating was tilted to cover the C IV emission line of each quasar and to overlap the B600 spectrum at approximately Ly  $\alpha$  emission.

To minimize slit losses from atmospheric dispersion, we designed observations to be taken as close to parallactic as possible. Almost all targets were placed near the centre of the slit to allow for accurate sky subtraction (flexure) and to still approximately minimize atmospheric dispersion when rotating the slit by  $180^\circ$  (Filippenko 1982). Typically, the two B600 exposures were taken with a  $10''$  spatial offset to mitigate CCD fringing at the reddest wavelengths after co-addition. Occasionally, limitations on guide star availability meant that targets could not be observed at parallactic angle or just with larger spatial offsets. However, cross-checks with the available SDSS spectra revealed that flux calibration was not compromised. We attribute part of this success to target acquisition in a filter near the wavelength range of interest (SDSS  $r$ ).

Throughout our programme we obtained GMOS baseline calibrations. One internal quartz halogen flat field exposure was attached to every science exposure, while wavelength calibration spectra were taken during daytime with a CuAr lamp. Night sky emission lines provided an approximate flexure correction. As per standard Gemini operating procedure, standard stars were observed at our various setups throughout each semester under varying conditions that still allowed for relative flux calibration. Bias frames were collected from the Gemini Science Archive.

More than half of the quasar spectra collected with GMOS-N in Semester 2010A were affected by local persistence on the EEV CCDs due to the standard practice to interleave GMOS science and

flat field exposures in queue observations. The persistence was stable and was corrected with dark exposures. Spatial offsets ensured that the remaining 2010A spectra did not fall close to affected pixels. In the following semesters GMOS-N science exposures were taken before any flat field exposures. Our GMOS-S sample does not show persistence effects.

Our survey was carried out in varying observing conditions to maximize schedulability and thus the final sample size. Our minimum acceptable conditions were: (i) image quality 85 percentile ( $\text{FWHM} \lesssim 1.1''$ ), (ii) sky background 50 percentile (dark-grey) and (iii) sky transparency 70 percentile (patchy clouds or cirrus). Eight of our targets received repeated observations due to clouds or bad seeing. All of these exposures were usually co-added to increase the S/N.

All of the spectra were processed in identical fashion using two software packages custom designed for Gemini/GMOS observations. Bias subtraction and flat fielding was performed using the GMOS package (v1.9) distributed by Gemini within the IRAF software platform. We found that the attached flat field frames showed constant fringing patterns independent of the telescope pointing, so for any given setup we combined the flat field frames to a high-quality master flat field and applied it to the data.

The remaining data reduction tasks were performed within the LOWREDUX software package<sup>1</sup> developed by J. Hennawi, D. Schlegel, S. Burles, and J. X. Prochaska. Wavelength solutions were generated from the CuAr arc lamp spectra, yielding typical RMS errors for the wavelength fits of  $\sim 0.3$  pixels, corresponding to  $\sim 0.6 \text{ \AA}$  and  $\sim 0.8 \text{ \AA}$  for the B600 and the R400 grating, respectively. The accuracy of the wavelength solutions is limited by instrument flexure and the almost critical sampling of the arc lines at the used spectral binning of four. Objects were automatically identified in each of the three sub-slits of the GMOS longslit and masked. Sky subtraction was performed on the remaining pixels. A global solution was performed first for each sub-slit and then a local refinement was made around each source in tandem with a spatial fit to the object profile. Each source was optimally extracted to produce a 1D spectrum, calibrated in wavelength. A sky spectrum was also extracted and compared to an archived solution based on the Paranal sky measurements (Hanuschik 2003) to estimate a rigid shift of the wavelength solution due to instrument flexure. We then corrected these values to vacuum and a heliocentric reference frame. The multiple exposures from the B600 grating were co-added, weighting by the S/N of the data (nearly identical in most cases). For the few quasars that were observed on multiple nights owing to variable observing conditions, we co-added all such data at this stage.

Standard stars observed throughout each semester were processed in identical fashion except spectral extraction which was performed with a 100 pixel boxcar. We compared these 1D extractions against catalogued spectra<sup>2,3</sup> to generate sensitivity functions that convert observed count rate to physical flux. After re-scaling to correct for non-photometric conditions, sensitivity functions of different standard stars taken throughout the survey showed an internal variation of less than 5 per cent. Telluric absorption could not be corrected due to the varying observing conditions and the lack of suitable standard stars. We corrected for atmospheric absorption using the average extinction curve for Mauna Kea

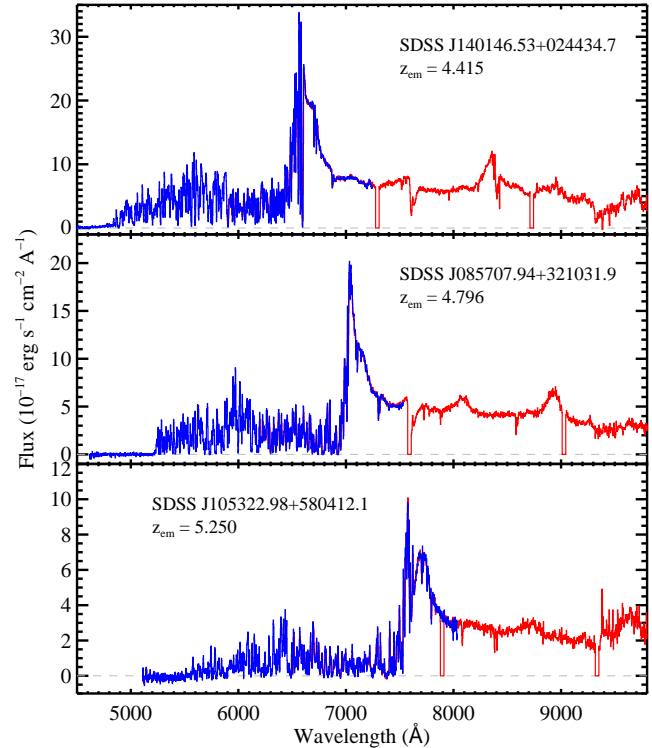


**Figure 2.** Gemini/GMOS spectra for three  $z_{\text{em}} > 4.4$  quasars drawn from the GGG survey. The blue lines indicate the data obtained with the B600 grating at a spectral resolution  $\text{FWHM} \approx 5.5 \text{ \AA}$ . The red lines, which overlap the blue data near Ly  $\alpha$ , trace the R400 grating observations ( $\text{FWHM} \approx 8.0 \text{ \AA}$ ). Gaps between detectors give the zero values in these red spectra. All spectra were fluxed using several spectrophotometric standard stars and scaled to the available SDSS spectra. See the online edition of the Journal for a colour version of this figure.

(Bèland, Boulade & Davidge 1988). Slit losses were corrected by scaling the GMOS spectra to the publicly available SDSS spectra of our targets in the regions where they overlap. Assuming negligible quasar variability between the epochs of observation, the resulting spectra have accurate absolute fluxes except at the ends of the covered spectral range of GMOS where the fitting errors in the sensitivity curves exceed a few per cent. The spectra collected at GMOS-S show fringing residuals at  $\lambda \gtrsim 8300 \text{ \AA}$  depending on the central wavelength. Finally, we corrected the spectra for Galactic extinction using the Cardelli, Clayton & Mathis (1989) extinction curve and the line-of-sight colour excess of Schlegel, Finkbeiner & Davis (1998).

Figure 2 shows the 1D spectra for three representative quasars from our GGG survey. Plots of all 163 quasar spectra are shown in Appendix A, available in the online edition of the Journal. All spectra are publicly available in reduced form<sup>4</sup>. The typical, absorbed S/N within the Ly  $\alpha$  forest is  $\sim 20$  per  $1.85 \text{ \AA}$  pixel,  $\sim 7$  times higher than in the SDSS discovery spectra. Due to the shorter exposure time with the R400 grating, the S/N at  $\lambda_r = 1450 \text{ \AA}$  is generally lower (Fig. 1), but still sufficient to accurately normalize the spectra.

The precise measurement of the mean free path at these high redshifts requires very accurate sky subtraction at the bluest wavelengths, i.e. below the Lyman limit of the quasar. Figure 3 shows

<sup>1</sup> <http://www.uchicago.edu/~xavier/LowRedux/index.html>

<sup>2</sup> <http://www.stsci.edu/hst/observatory/cdbs/calspec.html>

<sup>3</sup> <http://www.eso.org/sci/observing/tools/standards/spectra/stanlis.html>

<sup>4</sup> Link to VizieR will be provided upon acceptance of the manuscript.

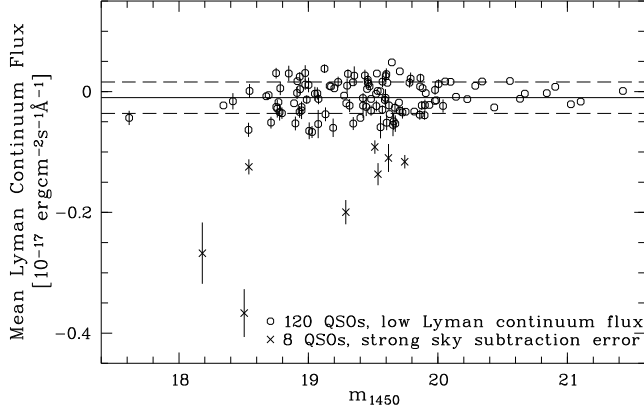


**Figure 3.** Mean Lyman continuum flux of the 128 quasars of our sample with a likely optically thick LLS vs. their apparent AB magnitude at  $\lambda_r = 1450 \text{ \AA}$ . Error bars are the standard error of the mean flux. Error bars smaller than the symbol size are not plotted. Crosses indicate the 8 quasars affected by systematic sky subtraction errors (significantly negative flux). The solid and dashed lines mark the average ( $-1 \times 10^{-19} \text{ erg cm}^{-2} \text{ s}^{-1} \text{ \AA}^{-1}$ ) and the standard deviation ( $2.6 \times 10^{-19} \text{ erg cm}^{-2} \text{ s}^{-1} \text{ \AA}^{-1}$ ), of the 120 remaining measurements, respectively.

the mean Lyman continuum flux of the 128 quasars in our sample with a likely optically thick LLS in the covered wavelength range, as determined by visual inspection of the 1D and 2D spectra. Eight quasars in our sample show significantly negative flux due to a systematic overestimation of the sky background, the level of which increases with quasar continuum flux. As the majority of these affected targets were taken in bad seeing, we attribute this effect to an underestimation of the object spatial profile during extraction, with a few per cent of quasar flux leaking into the sky subtraction windows. After excluding these outliers, we still estimate a slightly negative average flux ( $-1 \times 10^{-19} \text{ erg cm}^{-2} \text{ s}^{-1} \text{ \AA}^{-1}$ ) with considerable dispersion ( $2.6 \times 10^{-19} \text{ erg cm}^{-2} \text{ s}^{-1} \text{ \AA}^{-1}$ ). The residuals are generally less than 1 per cent of the quasar continuum flux redward of Ly  $\alpha$ . We include the systematic sky subtraction error in our analysis, but it does not significantly affect our results.

#### 4 REDSHIFT DETERMINATION

Our science goals are dependent on precise estimations of the quasar emission redshifts, especially analysis of the mean free path. It is now well appreciated that the standard approach taken by the SDSS to automatically estimate quasar redshifts gives values that are systematically in error (Richards et al. 2002; Hewett & Wild 2010). For this reason, several groups have developed algorithms to re-measure the values from resonant and fine-structure lines in the rest-frame far-UV (Shen et al. 2007; Hewett & Wild 2010).

To fully explore the aspects of this challenging problem, we have analysed the GGG spectra with several techniques and compare the results with estimates from the literature. Our first method was to estimate  $z_{\text{em}}$  ‘by-eye’, assuming that the peaks of suitable UV emission lines are located at their laboratory wavelengths. We focused especially on low-ionization emission lines (O I + Si II  $\lambda = 1303.49 \text{ \AA}$  and C II  $\lambda = 1335.30 \text{ \AA}$ ), which are believed to have small offsets from systemic (Tytler & Fan 1992; Vanden Berk et al. 2001). We refer to this approach as ‘GGG’. Redshift errors were estimated based on the emission line used, the presence of associated

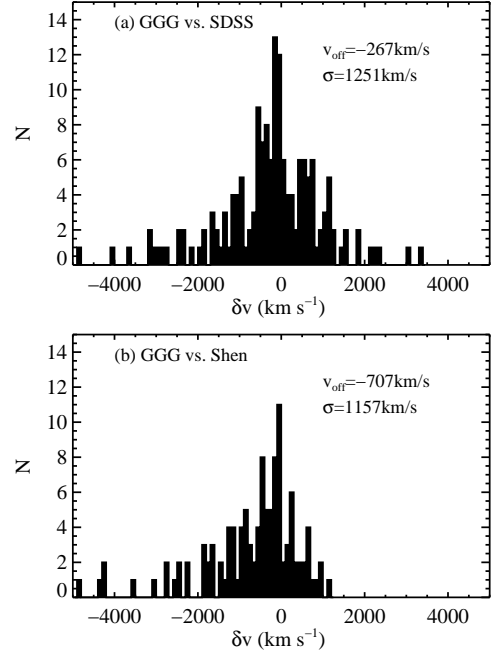


**Figure 4.** Comparison of the GGG quasar redshifts to other redshift estimates of our targets (see text). The tail to negative velocities in the lower panel arises because these quasars have very weak emission lines (Fig. 5) and, therefore, have redshifts best estimated from the onset of the Ly  $\alpha$  forest.

absorption (either BAL, narrow associated or atmospheric), the onset of the H I Ly  $\alpha$  forest, and the overall consistency between the suite of emission lines. The estimated uncertainty for these redshift measurements ranges from  $\sim 250$  to  $\sim 1000 \text{ km s}^{-1}$ . Table A2 summarizes the results of this method.

Secondly, we applied the semi-automated algorithm of Shen et al. (2007) to estimate  $z_{\text{em}}$ . This routine measures the centroids of each  $5\sigma$ -detected UV-emission line from the following: H I Ly  $\alpha$ , Si IV, C IV, and C III]. The algorithm then estimates  $z_{\text{em}}$  based on average velocity offsets measured from systemic, as gauged from [O III] nebular emission in lower redshift quasars. Each fit was visually inspected and modifications were occasionally made to the analysis (e.g. the elimination of a poorly-fit emission line). The lines analysed and the  $z_{\text{em}}$  estimates and uncertainties are listed in Table A2. We refer to this technique as ‘Shen’. Lastly, we list the best estimates from Hewett & Wild (2010) who applied an algorithm similar to that of Shen et al. (2007) to SDSS Data Release 6. We refer to those measurements as ‘HW’.

Figure 4a shows a histogram of the offsets in redshift between the GGG- $z_{\text{em}}$  measurements and the values reported in Schneider et al. (2010). There is a considerable scatter between the two sets of measurements ( $\sigma_v = 1250 \text{ km s}^{-1}$  or  $\sigma_z \approx 0.025$ ), but on average the GGG redshifts are only slightly higher than the SDSS redshifts (mean offset  $v_{\text{off}} \approx -270 \text{ km s}^{-1}$ ). In contrast, a comparison of the GGG- $z_{\text{em}}$  measurements with the Shen- $z_{\text{em}}$  values shows an  $\approx -700 \text{ km s}^{-1}$  offset driven by an asymmetric tail to negative velocities (Figure 4b). A comparison to the Hewett & Wild (2010) redshifts reveals a similar tail. In Figure 5 we show the four spectra with  $\delta v < -4000 \text{ km s}^{-1}$  between the GGG- $z_{\text{em}}$  and Shen- $z_{\text{em}}$  evaluations. Each case is marked by very weak Si IV and C IV emission as well as strong H I absorption just blueward of rest-frame Ly  $\alpha$ . These cases have had their GGG- $z_{\text{em}}$  values estimated from the onset of Ly  $\alpha$  forest

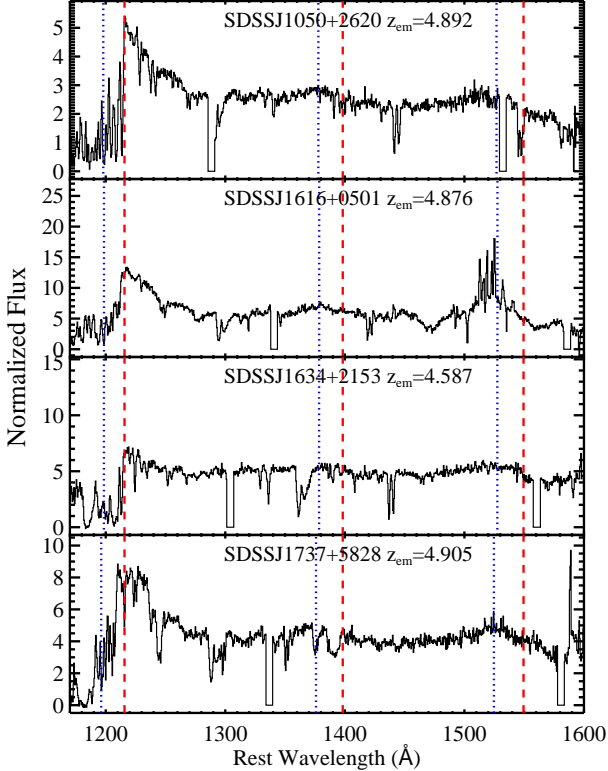


**Figure 5.** Gemini/GMOS R400 spectra of four quasars which have large differences in  $z_{em}$  from our analysis (which sets the rest wavelength here) and from using the Shen et al. (2007) algorithm. The vertical dashed lines indicate the rest wavelengths of H I Ly  $\alpha$ , Si IV, and C IV. The dotted lines show the positions for these emission lines when adopting the Shen estimate for  $z_{em}$ . The large offset occurs because these sources have very weak emission lines. Indeed, our preferred values come from analysis of the onset of the Ly  $\alpha$  forest. These values are adopted in the following mean free path analysis.

absorption, and we strongly prefer these values. After excluding outliers at  $\delta v < -2000 \text{ km s}^{-1}$ , the GGG vs. Shen- $z_{em}$  velocity offset distribution is approximately symmetric with a mean offset  $v_{off} \approx -380 \text{ km s}^{-1}$  and standard deviation  $\sigma_v \approx 700 \text{ km s}^{-1}$ . As almost all Shen- $z_{em}$  values are based on Si IV and C IV (Table A2), with the former being blended with O IV] and the latter showing a blueshift that increases with luminosity (Richards et al. 2011), we consider the GGG- $z_{em}$  values more reliable for our sample of very luminous quasars (Fig. 1).

In the following analysis we adopt a Gaussian redshift error distribution with zero mean and standard deviation  $\sigma_z = 0.01$  (corresponding to  $\sigma_v \approx 500 \text{ km s}^{-1}$  at  $z \approx 4.8$ ) for the entire sample. We show below that redshift errors do not significantly affect our results.

## 5 THE MEAN FREE PATH AT $Z \sim 5$

### 5.1 Stacked rest-frame quasar spectra

Our technique for estimating the mean free path is to analyse the average flux of a cohort of quasars at similar redshift and at rest wavelengths shortward of the Lyman limit. The decrease in observed flux is attributed to the integrated, average LL opacity of the universe and  $\lambda_{mfp}^{912}$  is defined to be the average distance from the source where a packet of photons suffers an  $e^{-1}$  attenuation. The

next subsection describes the formalism and modelling in greater detail.

Central to the analysis is the generation of average (‘stacked’) rest-frame quasar spectra which describe the mean flux of the background sources, as attenuated by intergalactic hydrogen blueward of their Ly  $\alpha$  emission line. Because we are interested foremost in the average properties of the H I absorption, each sight line is given equal weighting. Our parent sample is the 163 quasars observed in the GGG survey (Table A1). Of these, 9 sources were excluded from any further analysis due to strong BAL features, many of which were not obviously apparent in the SDSS discovery spectra. The spectrum of one source, SDSS J120102.01+073648.1, is contaminated by flux from a neighbouring source, presumably foreground to the quasar. An additional 8 sources were excluded due to systematic sky subtraction errors (Section 3). Therefore, the final sample for generating stacked rest-frame spectra totals 145 quasars with  $z_{em} > 4.4$ .

Following the algorithm described in O’Meara et al. (2013), we have generated stacked rest-frame quasar spectra in three redshift intervals designed to have roughly equal numbers of quasars:  $z_{em} = [4.4, 4.7]$ ,  $[4.7, 5.0]$ , and  $[5.0, 5.5]$  with average redshifts  $z_q = 4.56, 4.86$ , and  $5.16$  (the median  $z_q$  values are similar). The GMOS/B600 spectrum of each quasar was shifted to the rest-frame, normalized to have unit flux at rest-wavelength  $\lambda_r = 1450 \text{ \AA}$ , and then binned on to a fixed wavelength grid with a constant dispersion of  $0.45 \text{ \AA}$  per pixel. This dispersion is sufficiently large to contain at least one pixel from each of the original spectra; the mean is adopted when two or more of the original pixels fall within a given pixel of the new grid. By taking a straight average of all the processed quasar spectra in each redshift interval, we generate a stacked spectrum that weights each sight line equally. Weighting by S/N instead would introduce a bias towards sight lines without strong LL absorption.

Figure 6 shows the stacked spectra, plotted in a pseudo-observer frame  $\lambda_{pseudo} = (1 + z_q)\lambda_r$  for clarity of presentation. Each spectrum shows the rest-frame quasar continuum with readily visible Ly $\beta$  and Ly $\gamma$  emission after being absorbed by the IGM with an effective Lyman series optical depth  $\tau_{eff}^{Lyman}$  and additional Lyman continuum optical depth  $\tau_{eff}^{LL}$  at  $\lambda_r < 912 \text{ \AA}$  (e.g. Madau 1995; Meiksin 2006; Worseck & Prochaska 2011). At  $\lambda_r \approx 900 \text{ \AA}$ , we measure the scatter in the stack relative to a median smoothed version of  $\approx 7$  (30) per cent in the lowest (highest) redshift interval. This scatter arises from stochasticity in the IGM, not Poisson noise in the individual spectra.

To assess uncertainties in the measurements that follow, we have generated three sets of 2000 stacked spectra in each redshift interval. We start by estimating sample variance by randomly sampling the quasars, allowing for duplications. The upper panel of Fig. 7 presents the full cohort of spectra for the  $z_{em} = [4.4, 4.7]$  interval. We measure an RMS per pixel that ranges from  $\approx 10$  per cent of the flux at  $912 \text{ \AA}$  to  $\gtrsim 30$  per cent at  $850 \text{ \AA}$ . These exceed the pixel-to-pixel scatter in the stacked spectrum. To assess the effects of redshift uncertainty, we generated a set of 500 stacked spectra where  $z_{em}$  of each quasar was randomly offset from its measured value by a Gaussian deviate with  $\sigma_z = 0.01$ . The middle panel of Fig. 7 reveals that redshift error is a relatively minor source of uncertainty, especially compared to sample variance. Still, we have included the combined uncertainty of sample variance and redshift error by generating a set of 2000 stacked spectra by randomly sampling the quasars and varying  $z_{em}$  at the same time (Fig. 7; lower panel).



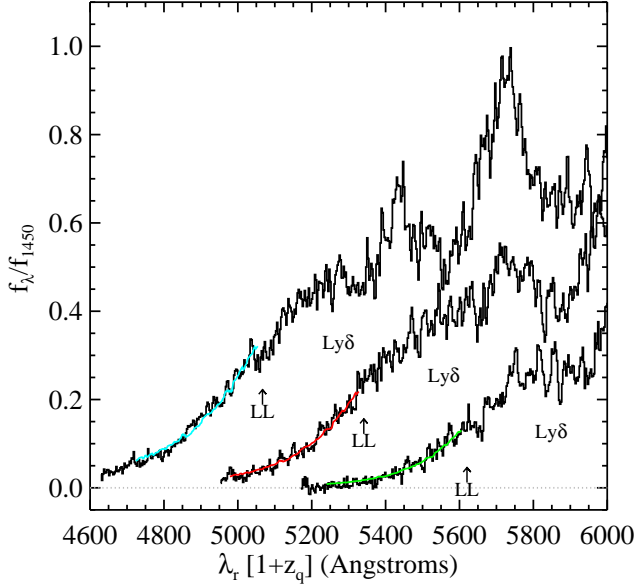


**Figure 6.** Stacked normalized rest-frame quasar spectra from the GGG survey generated for three redshift intervals:  $z_{\text{em}} = [4.4, 4.7]$ ,  $[4.7, 5.0]$ , and  $[5.0, 5.5]$ . These spectra are plotted in a pseudo-observer frame defined as  $\lambda_r (1 + z_q)$  with,  $z_q$  the average redshift of the quasars in each interval. The Ly $\delta$  emission (strongly affected by IGM absorption for the two high- $z$  bins) and the onset of the Lyman limit are marked for each stacked spectrum. Ly $\beta$  and Ly $\gamma$  emission lines of the background quasars are clearly visible. Overplotted on these stacked spectra are the best-fitting models which provide measurements for the mean free path  $\lambda_{\text{mfp}}^{912}$ .

## 5.2 Mean free path analysis and results

Using the stacked quasar spectra (Fig. 6), an estimation of the mean free path to ionizing photons is made by modelling the flux below the Lyman limit. This technique was developed and applied to  $z < 4$  quasars in previous works (Prochaska, Worseck & O’Meara 2009; O’Meara et al. 2013; Fumagalli et al. 2013b). Here, we refine the formalism to best match the nature of the IGM at  $z \sim 5$ .

We model the intrinsic flux of the quasar stack using the radio-quiet quasar SED of Telfer et al. (2002) modulated by a power-law and allowing for uncertainty in the normalization at 912 Å. We find that apart from an obvious Baldwin effect in the C IV emission line (e.g. Baldwin 1977; Richards et al. 2011), this is a very good match to the data redward of the Ly  $\alpha$  forest. At  $\lambda_r < 1215$  Å, the flux is attenuated by the Lyman series opacity beginning with Ly  $\alpha$  (i.e. an effective optical depth  $\tau_{\text{eff}}^{\text{Ly}\alpha}$ ). Below 912 Å, the flux is modulated by the full Lyman series effective optical depth  $\tau_{\text{eff}}^{\text{Lyman}}$  and the Lyman limit effective optical depth  $\tau_{\text{eff}}^{\text{LL}}$  (e.g. Madau 1995; Meiksin 2006; Worseck & Prochaska 2011). Explicitly, we may express the observed flux at these wavelengths as

$$f_{\lambda}^{\text{obs}} = f_{\lambda}^{\text{SED}} \exp(-\tau_{\text{eff}}^{\text{Lyman}}) \exp(-\tau_{\text{eff}}^{\text{LL}}), \quad (1)$$

where both  $\tau_{\text{eff}}^{\text{Lyman}}$  and  $\tau_{\text{eff}}^{\text{LL}}$  depend on redshift (and therefore wavelength; see below).

In practice, we model the observed flux below the Lyman limit relative to the observed flux at 912 Å (measured from the stacked spectrum) as

$$f_{\lambda < 912}^{\text{obs}} = f_{912}^{\text{obs}} \left( \frac{C_{912} f_{\lambda}^{\text{SED}}}{f_{912}^{\text{SED}}} \right) \times \exp(-[\tau_{\text{eff},\lambda}^{\text{Lyman}} - \tau_{\text{eff},912}^{\text{Lyman}}]) \exp(-\tau_{\text{eff}}^{\text{LL}}), \quad (2)$$

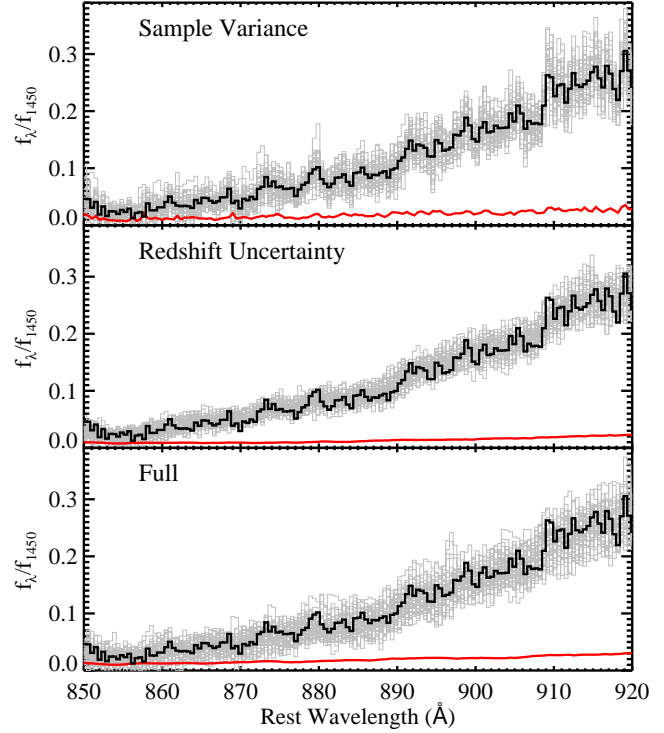


**Figure 7.** Bootstrap realizations of the rest-frame stacked spectrum for the  $z_{\text{em}} = [4.7, 5.0]$  cohort of quasars from the GGG survey. The top panel shows the stacks when one allows for duplications, i.e. it explores the effects of sample variance. The middle panel only allows for random offsets in  $z_{\text{em}}$  for each quasar. The lowest panel shows the combined effect of redshift error and sample variance. In all panels, the thick black curve shows the actual stacked spectrum, the grey curves show individual bootstrap realizations, and the lowest curve indicates the RMS of the bootstrap realizations as a function of wavelength. We find that the redshift uncertainty has a small effect, especially in comparison to that for sample variance.

with each of these quantities defined below.

Altogether, the model described by Equation 2 has four model parameters: (i) a nuisance parameter  $C_{912}$  for the overall normalization of the model. This accounts for uncertainty in evaluating  $f_{912}^{\text{obs}}$  from the stacked spectrum; (ii) a power-law tilt  $\delta\alpha_T$  applied to the assumed Telfer et al. (2002) SED, normalized at 1450 Å

$$f_{\lambda}^{\text{SED}} = \frac{f_{\lambda}^{\text{Telfer}}}{f_{1450}^{\text{Telfer}}} \left( \frac{\lambda}{1450 \text{ Å}} \right)^{\delta\alpha_T}; \quad (3)$$

(iii) an exponent  $\gamma_{\tau}$  which determines the redshift evolution of the effective optical depth from Lyman series absorption,

$$\tau_{\text{eff},\lambda}^{\text{Lyman}} = \tau_{\text{eff},912}^{\text{Lyman}} \left( \frac{1+z}{1+z_{912}} \right)^{\gamma_{\tau}}, \quad (4)$$

where  $z_{912} \equiv \lambda_r (1 + z_q) / (911.7621 \text{ Å}) - 1$ . In practice,  $\tau_{\text{eff},912}^{\text{Lyman}}$  is set to match the observed flux at 912 Å given the SED, i.e.  $\tau_{\text{eff},912}^{\text{Lyman}} = \ln(f_{912}^{\text{SED}} / f_{912}^{\text{obs}})$ ; (iv) an opacity  $\kappa_{912}$  describing the effective LL optical depth

$$\tau_{\text{eff}}^{\text{LL}}(z_{912}, z_q) = \kappa_{912} \frac{c}{H_0} (1 + z_{912})^{2.75} \times \int_{z_{912}}^{z_q} (1 + z')^{-5.25} dz'. \quad (5)$$

The exponents in Equation 5 are set by cosmology and an

adopted  $\nu^{-2.75}$  dependence for the photoionization cross-section (see Prochaska, Worseck & O’Meara 2009; O’Meara et al. 2013). Unlike previous works, we do not fit for redshift evolution in  $\kappa_{912}$  because we find it to be highly degenerate with the normalization when  $\lambda_{\text{mfp}}^{912} \ll 100h_70^{-1}$  Mpc.

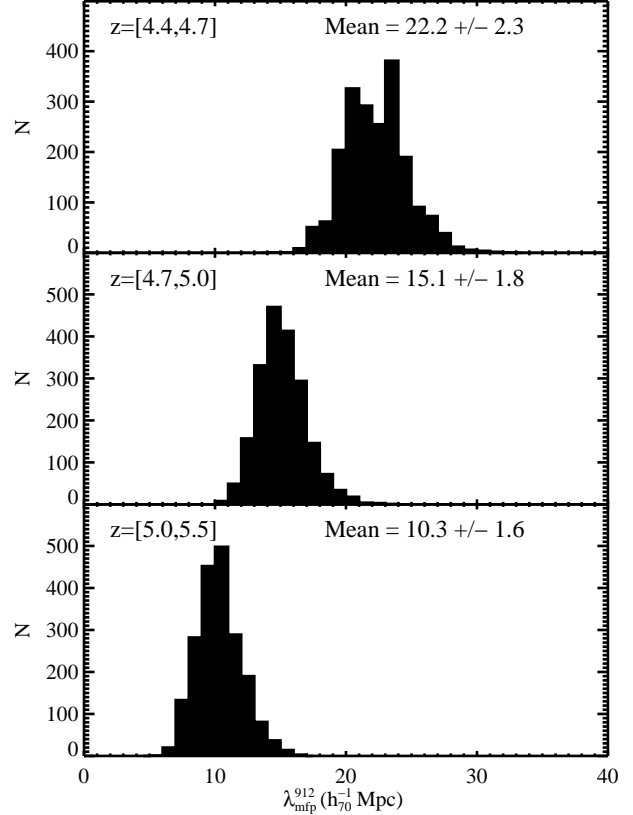
It is evident from Equation 2 that  $f_{\lambda}^{\text{obs}}$  at wavelengths just below 912 Å can change rapidly only if  $\tau_{\text{eff}}^{\text{LL}}$  is significant. Furthermore, unless one adopts an extreme tilt for the SED that is ruled out by observations ( $\delta\alpha_{\text{T}} > 0.5$ ), the LL opacity is the only factor which actually lowers  $f_{\lambda}^{\text{obs}}$ . Therefore, the sharp decline in flux observed in the stacked spectra at  $\lambda_{\text{r}} < 912$  Å (Fig. 6) must be driven by  $\tau_{\text{eff}}^{\text{LL}}$ , such that the model is most sensitive to  $\kappa_{912}$ . In fact, we find substantial degeneracy between the models if we attempt to constrain anything other than the normalization term  $C_{912}$  and  $\kappa_{912}$ . Therefore, we solved for these two model parameters and explore the dependency of the results on the other factors. For our fiducial models, we set  $\delta\alpha_{\text{T}} = 0$  and  $\gamma_{\tau} = 2.5$ , where the latter is motivated by observed redshift evolution in the Lyman series effective optical depth of the IGM (Becker et al. 2013; Prochaska et al. 2014). The model comparison to the data is performed at wavelengths  $\lambda_{\text{r}} = 850 - 910$  Å where  $\chi^2$  is minimized assuming  $\sigma_{\lambda} = 0.02$  which is characteristic of the scatter in the stacked spectrum. We caution that the stacked spectral fluxes are not truly independent and therefore values of  $\chi^2$  should not be interpreted in the standard fashion.

Figure 6 presents the best-fitting models for each stacked spectrum, which provide a good description of the observations ( $\chi_{\nu}^2 \lesssim 1$ ). From these models, we assess the effective redshift  $z_{912}^{\tau=1}$  where  $\tau_{\text{eff}}^{\text{LL}} = 1$  (Equation 5) and then measure  $\lambda_{\text{mfp}}^{912}$  as the proper separation between  $z_{912}^{\tau=1}$  and  $z_{\text{q}}$  with our assumed cosmology (Table 2). Uncertainties in the  $\lambda_{\text{mfp}}^{912}$  values were estimated from the 2000 stacked spectra generated with bootstrap techniques (§ 5.1; Fig. 7). These include the combined effects of redshift error and sample variance. Figure 8 presents the results of this analysis. The distributions of  $\lambda_{\text{mfp}}^{912}$  values are roughly Gaussian and we adopt the measured RMS as the statistical error in the  $\lambda_{\text{mfp}}^{912}$  values. These are 10–15 per cent of the central values.

There are at least four sources of systematic uncertainty in our models which affect the resultant  $\lambda_{\text{mfp}}^{912}$  values. Two of these relate to using models with assumed values for  $\delta\alpha_{\text{T}}$  and  $\gamma_{\tau}$ . The first two panels of Fig. 9 show the explicit dependence of the  $\lambda_{\text{mfp}}^{912}$  values (relative to the fiducial value) when  $\delta\alpha_{\text{T}}$  and  $\gamma_{\tau}$  are varied. The behaviour is as one expects, an increase (decrease) in  $\delta\alpha_{\text{T}}$  ( $\gamma_{\tau}$ ) implies lower flux for the models prior to including LL attenuation resulting in smaller  $\tau_{\text{eff}}^{\text{LL}}$  values (and larger  $\lambda_{\text{mfp}}^{912}$ ). The variations in  $\lambda_{\text{mfp}}^{912}$ , however, are small; for a plausible range of  $\delta\alpha_{\text{T}}$  and  $\gamma_{\tau}$  values there is a less than 5 per cent effect. We conclude that these two systematic errors are insignificant in comparison with sample variance.

In addition, we estimated the systematic error incurred due to the over-subtraction of the sky background level in our data set (Fig. 3). The lowest panel in Fig. 9 shows that a typical upward correction of  $10^{-19}$  erg cm $^{-2}$  s $^{-1}$  Å $^{-1}$  results in a  $\simeq 5$  per cent larger  $\lambda_{\text{mfp}}^{912}$  in the two higher redshift bins. This is simply due to the low flux at the end of the spectral range used for the fit of  $\lambda_{\text{mfp}}^{912}$  (Fig. 6).

Another source of systematic uncertainty relates to detailed fluctuations in the adopted SED, i.e. on  $\sim 5$  Å scales. These presumably arise from unresolved emission lines and also noise in the spectra analysed by Telfer et al. (2002). There is little reason to expect that this SED captures the true flux modulations in  $z_{\text{em}} \sim 5$  quasars. To explore the effect of small-scale variations in the SED,



**Figure 8.** Distribution of  $\lambda_{\text{mfp}}^{912}$  values measured from 2000 bootstrap realizations of the stacked spectra. The scatter is dominated by sample variance, e.g. fluctuations in the number of strong H I absorbers in the stacks. Each distribution is well-modelled by a Gaussian although we note the presence of a small tail to larger  $\lambda_{\text{mfp}}^{912}$  values.

we repeated our analysis allowing for 10 per cent fluctuations in the Telfer SED on 5 Å scales using a Gaussian deviate. From 500 trials in each composite we find a 10 per cent effect, comparable to the uncertainty from sample variance. In summation, we estimate that the magnitude of systematic uncertainty is comparable to the  $\approx 15$  per cent statistical error associated with sample variance and redshift error. This implies that future surveys would need to address these systematic effects to substantially improve upon our measurements.

## 6 DISCUSSION

### 6.1 Redshift evolution in the mean free path

Studies of the IGM across cosmic time have revealed redshift evolution in many properties of the Ly $\alpha$  forest: temperature (e.g. Lidz et al. 2010; Becker et al. 2011), line density (e.g. Kim et al. 2013), and the flux PDF (e.g. Becker, Rauch & Sargent 2007; Kim et al. 2007). Perhaps the best measured quantity has been the effective opacity of H I Ly $\alpha$   $\tau_{\text{eff}}^{\text{Ly}\alpha}$ , which numerous authors have found to decrease rapidly from  $z = 4$  to 2 (Kirkman et al. 2005; Faucher-Giguère et al. 2008; Dall’Aglio, Wisotzki & Worseck 2008; Pâris et al. 2011). A recent parametrization of the redshift evolution finds  $\tau_{\text{eff}}^{\text{Ly}\alpha}(z) = 0.751 [(1+z)/4.5]^{2.9} - 0.132$  (Becker et al. 2013). The steep evolution in  $\tau_{\text{eff}}^{\text{Ly}\alpha}$  is attributed to the expansion of the uni-



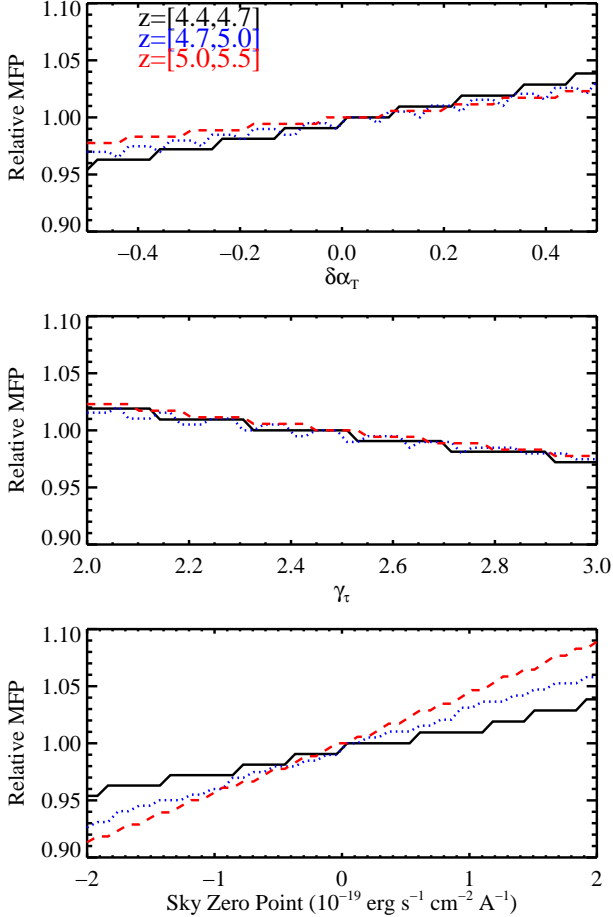


**Figure 9.** Dependence of  $\lambda_{\text{mfp}}^{912}$  on fixed model parameters. The panels plot the  $\lambda_{\text{mfp}}^{912}$  value measured relative to our fiducial estimate as one varies the tilt in the intrinsic quasar SED ( $\delta\alpha_{\text{T}}$ ; upper panel), the redshift evolution in the Lyman series effective optical depth ( $\gamma_{\text{T}}$ ; middle panel), or the sky zero point (lower panel). Our three subsamples are indicated by line style and colour ( $z_{\text{em}} = [4.4, 4.7]$ : black solid;  $z_{\text{em}} = [4.7, 5.0]$ : blue dotted;  $z_{\text{em}} = [5.0, 5.5]$ : red dashed). For a relatively broad range in  $\delta\alpha_{\text{T}}$  and  $\gamma_{\text{T}}$  we find a  $\lesssim 5$  per cent systematic dependence. Correction of the sky level zero point (Fig. 3) increases the  $\lambda_{\text{mfp}}^{912}$  values obtained from the  $z_{\text{em}} = [4.7, 5.0]$  and  $z_{\text{em}} = [5.0, 5.5]$  cohorts by  $\simeq 5$  per cent. See the online edition of the Journal for a colour version of this figure.

verse, an increase in the comoving number density of ionizing sources (quasars), and the decrease in the mean density of the gas which implies a lower hydrogen neutral fraction (e.g. Bolton & Haehnelt 2007; Davé et al. 2010). Several studies have also traced redshift evolution in the incidence of strong H I systems  $\ell(z)$ , e.g. damped Ly  $\alpha$  systems (DLAs) and LLSs, which are expected to trace non-linear and collapsed structures in the universe. Their incidences also decline rapidly towards lower redshift with  $\ell(z)$  scaling roughly as  $(1+z)^\eta$  for  $1 < \eta < 3$  (Prochaska, Herbert-Fort & Wolfe 2005; Prochaska, O’Meara & Worseck 2010; Rao, Turnshek & Nestor 2006; Songaila & Cowie 2010; Ribaudo, Lehner & Howk 2011). This exceeds the evolution attributable to cosmic expansion alone and implies a reduction in the filling factor of cool, dense gas in a given comoving volume. Including the results presented here, we have now measured the mean free path with the stacked spectrum technique from  $z \approx 2.5$  to  $\approx 5.2$  (Prochaska, Worseck & O’Meara 2009; O’Meara et al. 2013; Fumagalli et al. 2013b). By exploring

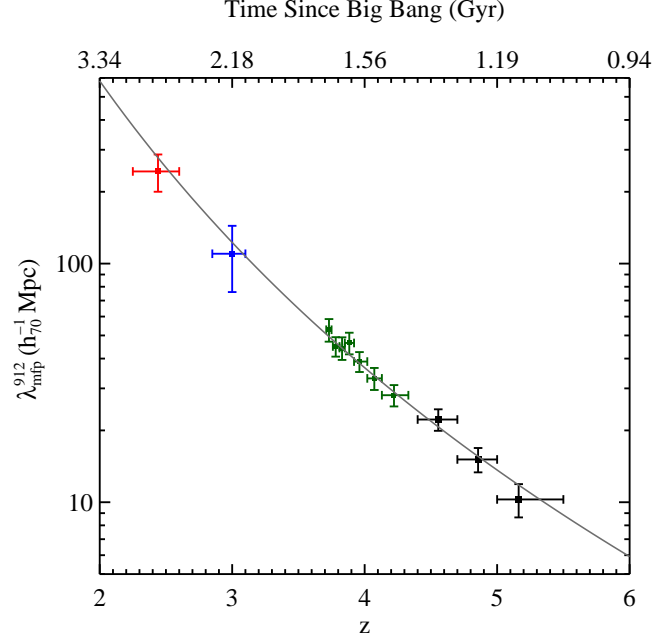


**Figure 10.** The proper mean free path to Lyman limit photons in the intergalactic medium as a function of redshift (and cosmic time). The data points show direct measurements via the spectral stacking technique as estimated in this manuscript (black), Prochaska, Worseck & O’Meara (2009, green), Fumagalli et al. (2013b, blue), and O’Meara et al. (2013, red). One observes a monotonic decrease with increasing redshift which is well modelled by a  $(1+z)^\eta$  power-law with  $\eta = -5.4 \pm 0.4$  (curve). See the online edition of the Journal for a colour version of this figure.

its redshift evolution, we may gain insight into the cosmological distribution of gas dominating the H I LL opacity<sup>5</sup>, its interplay with galaxies, and the formation/consumption of H I gas on cosmic scales. In turn, these results inform model predictions for evolution in the extragalactic UV background (Faucher-Giguère et al. 2009; Haardt & Madau 2012; Becker & Bolton 2013).

The complete set of  $\lambda_{\text{mfp}}^{912}$  values measured with our technique are presented in Fig. 10 and are listed in Table 2, each converted to the cosmology used in this manuscript<sup>6</sup>. It is evident that  $\lambda_{\text{mfp}}^{912}$  increases by over one order of magnitude from  $z = 5$  to 2.5. This must be driven in large part by the expansion of the universe. Therefore, one is motivated to model the redshift evolution in  $\lambda_{\text{mfp}}^{912}$  as a  $(1+z)^\eta$  power-law. Adopting a two-parameter model,  $\lambda_{\text{mfp}}^{912}(z) = A[(1+z)/5]^\eta$ , we minimize  $\chi^2$  under the assumption of Gaussian errors in the  $\lambda_{\text{mfp}}^{912}$  measurements (this assumption is not strictly true, but provides a good approximation, e.g. O’Meara et al. 2013). We find  $A = (37 \pm 2)h_{70}^{-1}$  Mpc and  $\eta = -5.4 \pm 0.4$  giving a reduced  $\chi_\nu^2 = 0.8$ . As is evident from Table 2, the SDSS measurements have the smallest estimated errors and therefore anchor the fit at  $z \approx 4$ . If we arbitrarily increase the uncertainty in these measurements, then  $\sigma(A)$  increases and  $\chi_\nu^2$  decreases but there is very little effect on  $\eta$  and its estimated uncertainty. Therefore, we conclude at high confidence that  $\lambda_{\text{mfp}}^{912}$  evolves

<sup>5</sup> Note that this likely includes gas that is both optically thick at the Lyman limit (e.g. LLSs, DLAs) and gas that has  $\tau_{912}^{\text{LL}} < 1$ .

<sup>6</sup> Note that for the SDSS measurements of Prochaska, Worseck & O’Meara (2009) we have modified the analysis to conform to the mean free path definition used here. This is a minor modification.

**Table 2.**  $\lambda_{\text{mfp}}^{912}$  Measurements.

$z_{\text{q}}$	$N_{\text{QSOs}}$	$\lambda_{\text{mfp}}^{912}$ [ $h_{70}^{-1}$ Mpc]	$\sigma(\lambda_{\text{mfp}}^{912})^*$ [ $h_{70}^{-1}$ Mpc]	Reference	Notes
Direct Measurements					
2.44	53	235.8	40.3	O’Meara et al. (2013)	
3.00	61	110.0	34.0	Fumagalli et al. (2013b)	Non-colour selected
3.73	150	52.8	5.7	Prochaska, Worseck & O’Meara (2009)	
3.78	150	45.0	4.2	Prochaska, Worseck & O’Meara (2009)	
3.83	150	44.3	4.8	Prochaska, Worseck & O’Meara (2009)	
3.88	150	46.5	4.8	Prochaska, Worseck & O’Meara (2009)	
3.96	150	38.9	3.7	Prochaska, Worseck & O’Meara (2009)	
4.07	150	33.0	3.5	Prochaska, Worseck & O’Meara (2009)	
4.22	150	28.1	2.9	Prochaska, Worseck & O’Meara (2009)	
4.56	57	22.2	2.3	This paper	
4.86	49	15.1	1.8	This paper	
5.16	39	10.3	1.6	This paper	
Indirect Estimates <sup>†</sup>					
3.0	$\sim 100$	85	65	Faucher-Giguère et al. (2008a)	LLSs and $\beta = 1.39, \gamma = 1.5$
3.5	$\sim 100$	49	20	Songaila & Cowie (2010)	LLSs and $\beta = 1.3, \gamma = 1.94$
4.5	$\sim 60$	20	8	Songaila & Cowie (2010)	LLSs and $\beta = 1.3, \gamma = 1.94$

Notes: All of the estimates have been translated to a common cosmology ( $\Omega_{\Lambda} = 0.7, \Omega_{\text{m}} = 0.3$  with  $H_0 = 70 \text{ km s}^{-1} \text{ Mpc}^{-1}$ ).

\*For the direct measurements, these are estimated from the RMS of 2000 bootstrap realizations of the stacked spectra.

<sup>†</sup>All of the indirect estimates are based on a measured incidence of LLSs combined with assumptions on the H I frequency distribution. The values listed are given at the redshift where the values were best estimated.

more steeply than  $(1+z)^{-4}$  at  $z < 5.5$ . We find a steeper redshift evolution than recovered for  $\tau_{\text{eff}}^{\text{Ly}\alpha}$ . Clearly, the astrophysics governing gas absorbing significantly at the LL differs from that of the canonical Ly  $\alpha$  forest.

Consider the physical significance of such strong evolution in  $\lambda_{\text{mfp}}^{912}$  with cosmic time. We assume first that the structures dominating the LL optical depth have a characteristic physical size  $D$  and comoving number density  $n_c$  at a given redshift. Under this assumption, the redshift evolution of the mean free path scales as

$$\lambda_{\text{mfp}}^{912} \propto \frac{(1+z)^{-3}}{\langle n_c D \rangle} \quad (6)$$

Therefore, in a universe where such structures do not evolve in comoving number density or physical size, one roughly predicts  $\lambda_{\text{mfp}}^{912} \propto (1+z)^{-3}$  from cosmological expansion<sup>7</sup>. This is strictly ruled out by the observations. Instead,  $\langle n_c D \rangle$  must decrease with time as approximately  $(1+z)^2$ . Whereas galaxies are assuredly growing in radius and number with decreasing redshift, structures dominating the LL opacity are *reduced* in number and/or physical size. This implies that the majority of such gas is not associated to the central regions of gravitationally collapsed structures (e.g. H I discs).

A possible scenario is that the LL opacity is dominated by gas in the haloes of galaxies (aka the circumgalactic medium or CGM) which then evolves across cosmic time. Numerical simulations of galaxy formation do predict a significant reservoir of cool, dense gas accreting on to galaxies via ‘cold streams’ that span the dark

matter haloes (Birnboim & Dekel 2003; Dekel & Birnboim 2006; Ocvirk, Pichon & Teyssier 2008; Dekel et al. 2009; Kereš et al. 2009; van de Voort et al. 2011). Portions of these streams are predicted to have significant LL opacity (Fumagalli et al. 2011; van de Voort et al. 2012) and should contribute to  $\tau_{\text{eff}}^{\text{LL}}$  at  $z > 2$ . These simulations also predict a declining covering fraction  $f_c$  of optically thick gas from these structures within the virial radius  $r_{\text{vir}}$  in time ( $r_{\text{vir}}$ ; Faucher-Giguère & Kereš 2011; Fumagalli et al. 2013a). On the other hand,  $r_{\text{vir}}$  is increasing and the physical cross-section remains roughly constant or even increases in galaxies of a given halo mass (Fumagalli et al. 2013a). Similarly, the central galaxies and the dark matter haloes only grow with cosmic time. Therefore, simple models for the evolution of optically thick gas in haloes could, in principle, predict a *decreasing* mean free path with decreasing  $z$ . Indeed, Fumagalli et al. (2013b) have argued that a significant fraction of LLSs with  $\tau_{912}^{\text{LL}} > 2$  must reside outside dark matter haloes at  $z > 3.5$ . We draw a similar inference for the gas dominating the H I LL opacity, which may hold to  $z < 3$ . For dark matter haloes to dominate the integrated LL opacity at high- $z$ , one may need to invoke scenarios where low mass haloes contribute a majority of the opacity at  $z \sim 5$  and then evaporate shortly after (e.g. mini-haloes; Abel & Mo 1998). Presently, we consider this to be an improbable scenario but we encourage the analysis of halo gas in lower mass haloes and also the properties of gas with  $\tau_{912}^{\text{LL}} < 1$  in all haloes.

We argue that the gas absorbing LL photons arises predominantly within large-scale structures near the collapsed regions of dark matter haloes (e.g. filaments, the cosmic web), consistent with current numerical results exploring the frequency distribution of H I gas (Fumagalli et al. 2011; McQuinn, Oh & Faucher-Giguère 2011; Altay et al. 2011; Rahmati et al. 2013) and recent analysis of the cross-correlation between LLSs and quasars (Prochaska et al. 2013). But what then drives the rapid evolution in  $\lambda_{\text{mfp}}^{912}$ ? There are three obvious possibilities: (i) the structures themselves decrease in physical size; (ii) their mass decreases; (iii) the gas becomes more highly ionized yielding lower LL opacity. We consider the first op-

<sup>7</sup> This scaling assumes that all opacity comes from highly optically thick absorbers and the mean free path is small. If, as we will argue below, absorbers with  $\tau_{912}^{\text{LL}} \lesssim 1$  significantly contribute to  $\lambda_{\text{mfp}}^{912}$  and the mean free path is large, cosmological expansion can lead to a redshift evolution that is steeper than  $(1+z)^{-3}$  due to redshifting of Lyman continuum photons (e.g. Becker & Bolton 2013). Redshift effects become significant at  $z \lesssim 3$  when  $\lambda_{\text{mfp}}^{912} \gtrsim 100 \text{ Mpc}$ .

tion to be very unlikely. If anything, structures outside dark matter haloes are likely to increase in size via cosmological expansion. There could be gravitational contraction along one dimension (possibly two), but this would be balanced by expansion in at least one other. The second effect, reduced mass, may follow from the funnelling of gas into galaxies and their haloes. In turn, this reduces the surface and volume densities of the gas. From  $z = 5$  to 2, the comoving mass density in dark matter haloes with  $M > 10^{10} M_{\odot}$  increases by a factor of 25. A significant fraction of the mass must come from the surrounding environment, but this could be replenished by new material from the even more distant IGM. We suspect that mass evolution is a sub-dominant effect for  $\lambda_{\text{mfp}}^{912}$  evolution but we encourage exploration in cosmological simulations on scales of a few  $r_{\text{vir}}$  around high- $z$  galaxies.

We posit that most structures giving rise to LL absorption are cosmologically expanding, yielding a lower density  $n_{\text{H}}$  that drives a substantial decrease in the H I fraction. Consider an idealized volume  $d^3$  of constant density  $n_{\text{H}}$  expanding with the universe. The average column density  $N_{\text{H}} \sim n_{\text{H}}d$  declines with time as  $(1+z)^2$  but the physical area of the structure increases by the same factor. Therefore, the average number of hydrogen nuclei that an ensemble of sight lines would intersect remains constant. The volume density evolves as  $(1+z)^3$ , however, and an optically thin medium bathed in radiation would see its neutral fraction lowered with time by the same scaling. Indeed, current estimates for the photoionization rate per hydrogen atom  $\Gamma_{\text{HI}}$  at  $z \sim 4$  based on measurements of the Ly  $\alpha$  opacity yield a nearly constant value (e.g. Faucher-Giguère et al. 2008a; Becker & Bolton 2013). We conclude that this effect dominates the rapid evolution in  $\lambda_{\text{mfp}}^{912}$ ; cosmological expansion alone can yield  $\eta < -5$  by reducing the effective physical size with substantial LL opacity.

This scenario requires that a significant fraction of the LL opacity comes from gas away from galaxies, i.e. with lower H I column densities. Indeed, Prochaska, O’Meara & Worseck (2010) and O’Meara et al. (2013) have inferred that  $\approx 50$  per cent of the opacity arises from gas with  $N_{\text{HI}} < 10^{17.5} \text{ cm}^{-2}$  (see also Rudie et al. 2013). Prochaska, O’Meara & Worseck (2010) also found that the observed decline in the incidence of LLSs is driven by gas with  $N_{\text{HI}} < 10^{19} \text{ cm}^{-2}$ . If this gas is more subject to the effects of cosmological expansion, one may predict significant evolution in the shape of the  $N_{\text{HI}}$  frequency distribution at  $N_{\text{HI}} < 10^{19} \text{ cm}^{-2}$  from  $z = 5$  to 2.5, consistent with recent numerical work (Rahmati et al. 2013).

Before concluding this sub-section, we note that at present, the data do not require a break in the power-law shown in Fig. 10. However, future studies at yet lower redshift (difficult to achieve) or improved statistics at  $2 < z < 3$  would test for such a break. This could indicate a change in the origin of optically thick gas on cosmological scales. Likewise, we caution against drawing firm conclusions from extrapolating our best-fitting power-law outside the covered redshift range ( $2.3 \lesssim z \lesssim 5.5$ ).

## 6.2 Comparison to models and implications for reionization

Despite recent progress it is still challenging to model LLSs in numerical simulations due to their small abundance in small simulation volumes, the involved high densities, necessary radiative transfer, and possible radiative feedback from local sources. Therefore, three approaches have been developed to model the IGM absorber population and the resulting  $\lambda_{\text{mfp}}^{912}$ : (i) empirical H I absorber statistics, (ii) semi-analytic additions to optically thin numerical simulations, and most recently (iii) cosmological simulations post-

processed with radiative transfer. Figure 11 presents a compilation of various estimates and compares them to our power-law fit derived in Section 6.1. We discuss these in the following.

The first approach uses an empirical parametrization for the H I absorber redshift and column density distribution  $f(N_{\text{HI}}, z)$  based on observations to calculate  $\tau_{\text{eff}}^{\text{LL}}(z_{912}, z_{\text{q}})$ , with  $\lambda_{\text{mfp}}^{912}$  defined as the distance at which  $\tau_{\text{eff}}^{\text{LL}}(z_{912}, z_{\text{q}}) \equiv 1$  (Table 2; Meiksin & Madau 1993; Madau, Haardt & Rees 1999; Faucher-Giguère et al. 2008a; Songaila & Cowie 2010; Haardt & Madau 2012; Rudie et al. 2013). Generally, these authors combined results on the observed incidence of LLSs with estimations or assumptions on the frequency of absorbers with  $N_{\text{HI}} \lesssim 10^{17} \text{ cm}^{-2}$ . They also adopted differing approaches to evaluating  $\lambda_{\text{mfp}}^{912}$  (e.g. whether to account for the redshifting of LL photons; see Becker & Bolton 2013). Recently, Prochaska et al. (2014) have examined systematic uncertainties related to evaluation  $\lambda_{\text{mfp}}^{912}$  via  $f(N_{\text{HI}}, z)$ . In addition to the difficulty in measuring  $f(N_{\text{HI}}, z)$  at  $N_{\text{HI}} \approx 10^{17} \text{ cm}^{-2}$  (e.g. Rudie et al. 2013; Kim et al. 2013), they identified two systematic effects related to the clustering of strong absorbers: (i) the double counting of structures absorbing LL photons which yields an underestimate of  $\lambda_{\text{mfp}}^{912}$ ; and (ii) a non-Poisson distribution of such absorbers which also increases  $\lambda_{\text{mfp}}^{912}$ . Given these issues and uncertainties, we consider it fortuitous that several of the previous  $\lambda_{\text{mfp}}^{912}$  estimations from  $f(N_{\text{HI}}, z)$  are in good agreement with our results (Fig. 11). Nevertheless, going forward we intend to combine our constraints on  $\lambda_{\text{mfp}}^{912}$  with measurements of  $f(N_{\text{HI}}, z)$  to explore the clustering and large-scale distributions of optically thick gas. We also note that our power-law fit is steeper than any previous empirical estimate due to our accounting for redshift effects at  $z < 3$  and the large redshift range now covered by our direct measurements.

Besides the above empirical estimates, optically thick systems can be added to the absorber frequency distribution obtained from optically thin numerical simulations, either based on their observed frequency (Meiksin & White 2004) or by semi-analytic approximations (Miralda-Escudé, Haehnelt & Rees 2000; Bolton & Haehnelt 2007). Specifically, Meiksin & White (2004) added the observed number of LLSs from Stengler-Larrea et al. (1995) (extrapolated to  $z > 4$ ) to their particle mesh simulations and obtained  $\lambda_{\text{mfp}}^{912} = 28 [(1+z)/5]^{-4.2} \text{ Mpc}$  at  $2.75 < z < 5.5$  for our adopted cosmology. In the redshift range considered by Meiksin & White (2004) we find reasonable agreement with the direct  $\lambda_{\text{mfp}}^{912}$  measurements from quasar stacks, again probably limited by the uncertainty in the parametrization of LLSs. Some physical insight may be gained by considering the Miralda-Escudé, Haehnelt & Rees (2000) model of a two-phase IGM composed of low-density fully ionized gas at  $\Delta = \rho/\bar{\rho} < \Delta_i$  and optically thick neutral clumps at  $\Delta > \Delta_i$ . With this approximate treatment of self-shielding and ignoring redshifting of the photons, the mean free path is the mean distance between the neutral clumps

$$\lambda_{\text{mfp}}^{912} = \lambda_0 F_{\Delta_i}^{-2/3} \quad , \quad (7)$$

with the H I volume filling fraction  $F_{\Delta_i}$  given by the density distribution function  $P(\Delta)$  as

$$F_{\Delta_i} = \int_{\Delta_i}^{\infty} P(\Delta) d\Delta \quad . \quad (8)$$

At low densities Miralda-Escudé, Haehnelt & Rees (2000) parametrized  $P(\Delta)$  using a hydrodynamical simulation (Miralda-Escudé et al. 1996), whereas at high densities below the resolution limit of the simulation  $P(\Delta)$  asymptotes to a power-law density profile. Miralda-Escudé, Haehnelt & Rees (2000) normal-

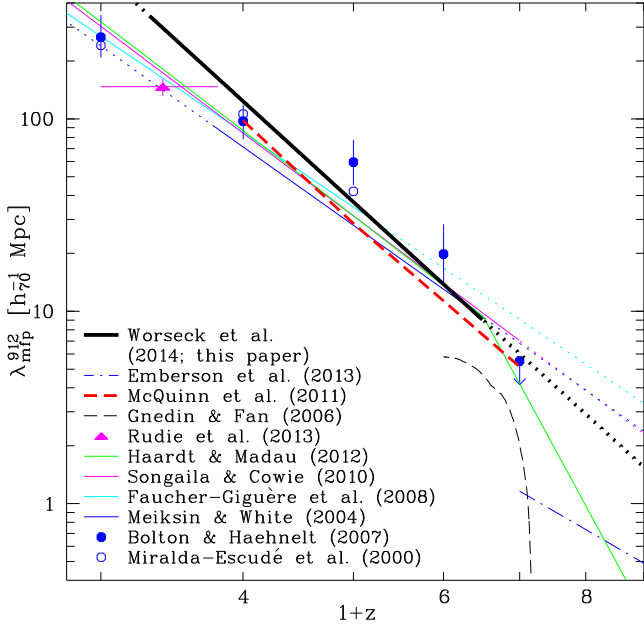


**Figure 11.** Comparison of various evaluations of the proper mean free path to Lyman limit photons. Power-law fits  $\lambda_{\text{mfp}}^{912} \propto (1+z)^n$  are shown as straight solid (dotted) lines in (outside) the quoted redshift range of validity. We show our power-law fit (thick black) and previous estimates based on H I absorber statistics (Faucher-Giguère et al. 2008a; Songaila & Cowie 2010; Haardt & Madau 2012; Rudie et al. 2013), semi-analytic additions to optically thin numerical simulations (Miralda-Escudé, Haehnelt & Rees 2000; Meiksin & White 2004; Bolton & Haehnelt 2007), and estimates obtained in a fully numerical framework (Gnedin & Fan 2006; McQuinn, Oh & Faucher-Giguère 2011; Emberson, Thomas & Alvarez 2013). See the text for a discussion. A colour version of this figure is shown in the online edition of the Journal.

ized the mean free path by noting that  $\lambda_0 H(z) \simeq 60 \text{ km s}^{-1}$  reproduces the scales of the Ly $\alpha$  forest in their simulation. Calibrating  $\Delta_i$  with the observed Ly $\alpha$  forest effective optical depth and the density distribution from their simulation, they obtained  $\lambda_{\text{mfp}}^{912}(z) \simeq (241, 106, 42) h_{70}^{-1} \text{ Mpc}$  at  $z = (2, 3, 4)$ . Despite the outdated cosmological parameters of the Miralda-Escudé et al. (1996) simulation, the latter two  $\lambda_{\text{mfp}}^{912}$  values are in very good agreement with the direct measurements (Prochaska, Worseck & O’Meara 2009; Fumagalli et al. 2013b). At  $z = 2$ , Equation 7 underpredicts  $\lambda_{\text{mfp}}^{912}$  due to redshift effects in the expanding universe (Miralda-Escudé, Haehnelt & Rees 2000). Bolton & Haehnelt (2007) slightly varied this approach by estimating the critical density for self-shielding analytically, and extrapolating the Miralda-Escudé, Haehnelt & Rees (2000) density distribution to  $z = 6$ . Their estimated  $\lambda_{\text{mfp}}^{912}$  values at  $z = 4$  and  $z = 5$  are  $\sim 50$  per cent larger than ours, probably due to the strong assumptions of the Miralda-Escudé, Haehnelt & Rees (2000) model (extrapolated density distribution, two-phase IGM, fixed  $\lambda_{\text{mfp}}^{912}$  normalization).

With these caveats in mind, we can combine the  $\lambda_{\text{mfp}}^{912}$  parametrization of Miralda-Escudé, Haehnelt & Rees (2000) and our power-law fit to  $\lambda_{\text{mfp}}^{912}(z)$  to estimate the H I volume filling fraction, yielding  $F_{\Delta_i} \approx 2.3 \times 10^{-4} [(1+z)/5]^{5.85}$ . Within the simplified framework of the Miralda-Escudé, Haehnelt & Rees (2000) model, this order-of-magnitude estimate confirms that the IGM is highly ionized at  $z < 5.5$ . Extrapolating the Miralda-Escudé, Haehnelt & Rees (2000) parametrization and our

fit of  $\lambda_{\text{mfp}}^{912}(z)$  to higher redshifts, we obtain  $F_{\Delta_i} \approx 2 \times 10^{-3}$  at  $z = 6$ , indicating that H I reionization likely occurred at  $z \gg 6$ . Adopting the density distribution of Miralda-Escudé, Haehnelt & Rees (2000) we use Equation 8 to obtain an approximate density threshold for self-shielding gas of  $\Delta_i \approx 300$  ( $\Delta_i \approx 100$ ) at  $z = 3$  ( $z = 4$ ). Assuming local hydrostatic equilibrium and typical values for the gas temperature and the UV background, these thresholds correspond to column densities remarkably similar to  $\tau_{912}^{\text{LL}} \simeq 1$  LLSs (Schaye 2001; Furlanetto & Oh 2005). While this is a good consistency check, we caution that  $\tau_{912}^{\text{LL}} \simeq 1$  LLSs are translucent, requiring radiative transfer models. Setting  $\Delta_i$  as the characteristic density of  $\tau_{912}^{\text{LL}} = 1$  LLSs (Bolton & Haehnelt 2007) neglects  $\tau_{912}^{\text{LL}} < 1$  absorbers and overestimates the number of optically thick ones.

Recent cosmological simulations post-processed with radiative transfer calculations have significantly improved upon semi-analytic models of optically thick gas (McQuinn, Oh & Faucher-Giguère 2011; Altay et al. 2011; Rahmati et al. 2013). These studies predict an H I column density distribution shaped by radiative transfer, smoothly transitioning from the optically thin IGM to fully neutral gas in the vicinity of galaxy haloes. Self-shielding is significant at high overdensities, in good agreement with our rough estimates obtained with the Miralda-Escudé, Haehnelt & Rees (2000) formalism. In particular, McQuinn, Oh & Faucher-Giguère (2011) self-consistently calculated the mean free path of LL photons from their simulations. Figure 11 shows  $\lambda_{\text{mfp}}^{912}(z)$  for their assumed power-law UV background spectrum  $J_\nu \propto \nu^{-1}$  yielding a UV background photoionization rate  $\Gamma_{\text{HI}} = 5 \times 10^{-13} \text{ s}^{-1}$ . A power-law fit to their values (M. McQuinn, priv. comm.) yields  $\lambda_{\text{mfp}}^{912} = 29.1 [(1+z)/5]^{-5.26}$  at  $3 \leq z \leq 6$ . Interestingly, the power-law exponent is almost identical to the one we obtain from the quasar stacks (Section 6.1), but their lower normalization results in a  $\sim 20$  per cent smaller mean free path at all redshifts (Fig. 11). For isothermal density profiles the Miralda-Escudé, Haehnelt & Rees (2000) model yields  $\Gamma_{\text{HI}} \propto [\lambda_{\text{mfp}}^{912}]^{1.5}$  (Furlanetto & Oh 2005) which approximately holds in the numerical treatment by McQuinn, Oh & Faucher-Giguère (2011). Thus, our independent mean free path measurements imply a UV background photoionization rate  $\Gamma_{\text{HI}} \approx 7 \times 10^{-13} \text{ s}^{-1}$  at  $z = 4$ , which agrees with current estimates at the  $1\sigma$  level (e.g. Becker & Bolton 2013). More importantly, as  $\Gamma_{\text{HI}} = \text{const.}$  in the simulation by McQuinn, Oh & Faucher-Giguère (2011), the similarly steep redshift evolution of the mean free path implies that  $\Gamma_{\text{HI}}$  should only weakly depend on redshift, in agreement with independent estimates from the Ly $\alpha$  forest (Faucher-Giguère et al. 2008a; Becker & Bolton 2013). Remaining tension in the shape of  $f(N_{\text{HI}}, z)$  between observations and the McQuinn, Oh & Faucher-Giguère (2011) simulation can be alleviated by a softer UV background spectrum (Altay et al. 2011; Rahmati et al. 2013). We encourage further numerical work on  $f(N_{\text{HI}}, z)$  with varying SEDs of the UV background calibrated to  $\Gamma_{\text{HI}}$  and  $\lambda_{\text{mfp}}^{912}$ .

At the highest redshifts  $z > 5$ , i.e. in the immediate post-reionization IGM, most previous inferences on the mean free path are brazen extrapolations from lower redshifts, leaving very few constraints that are based on actual measurements. At  $z = 6$  Bolton & Haehnelt (2007) give an upper limit  $\lambda_{\text{mfp}}^{912} < 5.5$  proper Mpc (corrected to our cosmology) based on H I Gunn-Peterson optical depth measurements (Songaila 2004; Fan et al. 2006) and the Miralda-Escudé, Haehnelt & Rees (2000) model extrapolated to  $z = 6$ . At the same redshift the power-law fit to the LLS in-

cidence by Songaila & Cowie (2010) yields  $\lambda_{\text{mfp}}^{912} \simeq 7 \text{ Mpc}$ , but with an estimated uncertainty of  $\sim 30$  per cent due to the poorly constrained shape of  $f(N_{\text{HI}}, z)$  at high redshift. Therefore it remains unclear whether their somewhat higher LLS incidence at  $5 < z < 6$  might correspond to a drop in  $\lambda_{\text{mfp}}^{912}$ . Likewise, the accuracy of our mean free path measurement from the GGG  $z_{\text{em}} > 5$  quasar stack is likely limited by sky subtraction errors and uncertainties in the adopted quasar SED (Section 5.2). Current quasar samples are too small to track rapid evolution in the mean free path at  $z > 5$ , so that the power-law parametrization from Section 6.1 is adequate. Extrapolating our fit by  $\Delta z = 0.5$  beyond the range of validity, we obtain  $\lambda_{\text{mfp}}^{912} = (6.0 \pm 0.9) \text{ Mpc}$  at  $z = 6$ , in very good agreement with Songaila & Cowie (2010).

The mean free path in the post-reionization IGM is an important boundary condition for H I reionization models. While in the early stages of H I reionization the mean free path strongly depends on the source properties as the ionizing photons are absorbed within individual H II regions, it is predicted to rise rapidly by several orders of magnitude as H II regions merge and reionization is completed (Gnedin 2000). After overlap the remaining high-density regions are gradually ionized, corresponding to a smoothly increasing mean free path. Hydrodynamical simulations of reionization with approximate radiative transfer and sufficiently large dynamic range predict the post-reionization mean free path to within a factor of  $\sim 2$ , limited either by box size (Gnedin 2000; Gnedin & Fan 2006) or sub-cell physics (Kohler, Gnedin & Hamilton 2007). As an example, Fig. 11 shows the mean free path evolution of the L8N256 run from Gnedin & Fan (2006), with an overlap epoch (and hence a large jump in  $\lambda_{\text{mfp}}^{912}$ ) at  $z \simeq 6.2$  by construction. Recently, Emberson, Thomas & Alvarez (2013) presented adiabatic hydrodynamical simulations post-processed with radiative transfer to predict the redshift evolution of the mean free path for different amplitudes of the UV background. For characteristic values of the UV background at  $z \sim 6$  ( $\Gamma_{\text{HI}} \simeq 3 \times 10^{-13} \text{ s}^{-1}$ ; e.g. Calverley et al. 2011) they underestimate the mean free path by a factor of  $\simeq 5$  (Fig. 11), at least in part due to their neglect of photoheating that would boost the mean free path by suppressing structure formation. In semi-numerical approaches to study the large-scale morphology of reionization the mean free path is an input parameter to impede the growth of H II regions, resulting in an extended reionization epoch and a spatially inhomogeneous UV background (Crociani et al. 2011; Alvarez & Abel 2012). Our measurements rule out very large and redshift-independent mean free paths for absorption systems assumed by Alvarez & Abel (2012).

Our  $\lambda_{\text{mfp}}^{912}$  measurements also constrain models for spatial fluctuations in the UV background in the post-reionization IGM. Adopting our power-law model, a spherical volume with radius  $r = \lambda_{\text{mfp}}^{912}$  contains roughly (11000, 1300, 180)  $M_{\text{UV}} < 0.9 M_{\text{UV}}^*$  star-forming galaxies at  $z = (5, 6, 7)$  (e.g. Bouwens et al. 2012). Due to the steep faint-end slope of the galaxy luminosity function, even a slight extrapolation beyond this currently observable magnitude limit would dramatically boost the average number of galaxies in this attenuation volume, arguing for a fairly homogeneous UV background at  $z \lesssim 6$  if such galaxies dominate the photon budget. However, galaxy clustering likely increases small-scale fluctuations in the UV radiation field, requiring numerical approaches (Mesinger & Furlanetto 2009).

### 6.3 Impact of quasar proximity zones

In the highest redshift interval considered ( $z_{\text{em}} > 5$ ), we measure a central value for the mean free path of only  $\lambda_{\text{mfp}}^{912} \simeq 10 \text{ Mpc}$ . This

implies, at least crudely, that a significant fraction  $f$  of sources will be strongly attenuated by gas within only a few Mpc. For example, we estimate that  $f(< 3 \text{ Mpc}) = 1 - \exp(-3 \text{ Mpc}/\lambda_{\text{mfp}}^{912}) \approx 25$  per cent of the sight lines will be strongly attenuated by gas within  $r = 3 \text{ Mpc}$  of the source. Such gas occurs within the so-called proximity zones of the quasars. On these scales, there are at least two effects which influence the characteristics of the H I gas that differ from random regions of the cosmological volume. First, quasars reside in massive galaxies (e.g. White et al. 2012) which themselves lie within large dark matter overdensities relative to the cosmic mean. Indeed, observations of projected quasar pairs at  $z \sim 2-3$  reveal excess H I absorption to beyond  $1 h_{70}^{-1} \text{ Mpc}$  transverse to the foreground quasar (Font-Ribera et al. 2013; Prochaska et al. 2013). Similarly, one measures a strong clustering signal between quasars and optically thick gas (Hennawi & Prochaska 2007; Prochaska, Hennawi & Simcoe 2013; Prochaska et al. 2013). Therefore, gas within the proximity zone apparently has large ‘intrinsic’ opacity to LL photons. On the other hand, the ionizing radiation emitted by the quasar illuminates the gas along our sight line and can photoionize the foreground H I to great distances (e.g. Hennawi & Prochaska 2007). Such a proximity effect is observed in the optically thin Ly  $\alpha$  forest (e.g. Scott et al. 2000; Dall’Aglio, Wisotzki & Worseck 2008; Calverley et al. 2011). The interplay of these two effects is obviously complex and depends at least upon the mass of the host galaxy and luminosity of the quasar (e.g. Faucher-Giguère et al. 2008b). In fact, one measures a lower incidence of optically thick LLSs within the proximity zones of  $z_{\text{em}} \sim 4$  quasars (Prochaska, O’Meara & Worseck 2010).

At  $z \sim 5$ , the incidence of such ‘proximate’ LLSs (PLLSs) has not yet been measured; this will be considered in a future paper of our series. We report here on preliminary results finding 13 cases of strong quasi-continuous absorption in the Lyman continuum at redshifts consistent with  $r < 3 \text{ Mpc}$  from the quasar. This represents one third of the  $z_{\text{em}} > 5$  quasar sample, consistent with our expectation based on the  $\lambda_{\text{mfp}}^{912}$  analysis, although we emphasize that these sight lines have contributed to the  $\lambda_{\text{mfp}}^{912}$  measurement. A refined treatment estimating the luminosity-dependent size of the proximity zone at which the photoionization rate of the quasar equals that of the UV background (e.g. Calverley et al. 2011) yields very similar results: The measured mean free path is just  $\simeq 1.8$  times larger than the average proximity zone size  $r_{\text{prox}} \simeq 6 \text{ Mpc}$  of the targeted  $z_{\text{em}} > 5$  quasars. At present, any such analysis is limited by quasar redshift uncertainty ( $\sigma_r \simeq 1 \text{ Mpc}$ ), strong contaminating Lyman series absorption at lower redshifts, and the uncertainty in the likely evolving UV background at  $z > 5$  (Calverley et al. 2011). The high incidence of PLLSs at  $z > 5$  is consistent with an extrapolation from  $z \lesssim 4$  (Prochaska, O’Meara & Worseck 2010). While  $\lambda_{\text{mfp}}^{912}$  at  $z < 4$  is sufficiently large that gas in the proximity zone provides  $\lesssim 10$  per cent of the effective optical depth (Prochaska, O’Meara & Worseck 2010; O’Meara et al. 2013; Fumagalli et al. 2013a), our measurements at  $z > 5$  are influenced by gas local to the quasar. We can estimate this potential bias by adopting the power-law parametrization for  $\lambda_{\text{mfp}}^{912}(z)$  at  $z < 5$  and comparing the extrapolated  $\lambda_{\text{mfp}}^{912}$  at  $z > 5$  to the measured value. The fit to  $z < 5$  yields  $\lambda_{\text{mfp}}^{912}(z) = (37 \pm 2) [(1+z)/5]^{-5.3 \pm 0.5} \text{ Mpc}$  at a reduced  $\chi^2_{\nu} = 0.3$ , consistent with the fit to all data. The extrapolated mean free path at the mean redshift of the  $z_{\text{em}} > 5$  stack ( $z_q = 5.16$ ) agrees with the measured value within  $1\sigma$ , suggesting that proximity zones do not strongly bias our  $\lambda_{\text{mfp}}^{912}$  measurement.

However, measuring a mean free path that approaches the

quasar proximity zone size has several important implications. First, our results on  $\lambda_{\text{mfp}}^{912}$  at  $z > 5$  may not apply to the ‘random’ IGM. If the proximity zones of these quasars have a higher (or lower) incidence of optically thick gas, this will bias the  $\lambda_{\text{mfp}}^{912}$  values accordingly relative to the cosmological average at that epoch. On the other hand, ionizing sources do not inhabit a random distribution of the universe, but must occur within collapsed, overdense structures. Furthermore, the majority of optically thick gas is almost surely associated to galaxies and their surrounding environments (e.g. Fumagalli et al. 2011; McQuinn, Oh & Faucher-Giguère 2011; van de Voort et al. 2012) and also biased relative to random regions. Therefore, while  $\lambda_{\text{mfp}}^{912}$  measurements from quasars may be biased evaluations they are obviously valid for assessing the attenuation of Lyman continuum photons emitted by luminous  $z_{\text{em}} \sim 5$  quasars. It is unknown, however, how optically thick gas is clustered to fainter quasars and/or star-forming galaxies at that epoch and approaching reionization. Thus, the mean free path at  $z > 5$  likely depends on the source environment and cannot be regarded as the mean separation between LLSs in the IGM (that interpretation holds only for diffuse Lyman continuum photons from recombination). Furthermore, clustering of the sources and absorbers requires a more sophisticated treatment than simple Poisson statistics (Prochaska et al. 2014).

Another implication is that  $z \simeq 5.2$  currently marks the highest redshift at which  $\lambda_{\text{mfp}}^{912}$  measurements from stacked quasar spectra can be safely related to the IGM. At  $z > 5.5$  the mean free path is smaller than the typical proximity zone size of luminous quasars (see also Calverley et al. 2011), such that any stacking analysis should be restricted to fainter quasars or star-forming galaxies with smaller proximity zones. Alternatively,  $\lambda_{\text{mfp}}^{912}$  estimates may be obtained from the incidence of intervening LLSs assuming the shape of the column density distribution, but this remains a challenging task at  $z > 5$  (Songaila & Cowie 2010).

## 7 CONCLUSIONS

We have presented first results from the Giant Gemini GMOS (GGG) survey of the intergalactic medium at  $z \gtrsim 4$ . In a long-term multi-partner Gemini programme we have obtained high-quality ( $S/N \sim 20$  per  $1.85 \text{ \AA}$  pixel) low-resolution ( $\text{FWHM} \approx 320 \text{ km s}^{-1}$ ) spectra of 163  $z_{\text{em}} > 4.4$  quasars, the largest sample of its kind at these redshifts. The reduced data are publicly available<sup>8</sup>. The primary goal of this survey has been a precise measurement of the mean free path to H I Lyman limit photons in the high-redshift universe via the analysis of stacked rest-frame quasar spectra, a technique pioneered by our team (Prochaska, Worseck & O’Meara 2009). Future papers in this series will determine the incidence rate of DLAs and LLSs at  $z > 4$  and, by using the total Lyman limit opacity determined from the mean free path, constrain the column density distribution of  $\tau_{912}^{\text{LL}} < 1$  absorbers. Our primary results are as follows:

(i) The mean free path  $\lambda_{\text{mfp}}^{912}$  monotonically decreases with redshift. Subsampling our data set we measure  $\lambda_{\text{mfp}}^{912} = (22.2 \pm 2.3, 15.1 \pm 1.8, 10.3 \pm 1.6) h_{70}^{-1}$  proper Mpc (68 per cent confidence level) at mean redshifts of the stacks  $z_{\text{q}} = (4.56, 4.86, 5.16)$ , respectively (Figs. 6 & 8).

(ii) When combining these measurements with lower-redshift results obtained with the stacking technique

(Prochaska, Worseck & O’Meara 2009; O’Meara et al. 2013; Fumagalli et al. 2013b), we find that the mean free path smoothly evolves between  $z = 2.3$  and  $z = 5.5$  (Fig. 10), well described by a power-law:  $\lambda_{\text{mfp}}^{912}(z) = A[(1+z)/5]^\eta$  with  $A = (37 \pm 2) h_{70}^{-1} \text{ Mpc}$  and  $\eta = -5.4 \pm 0.4$  (68 per cent confidence level).

The redshift evolution of the mean free path exceeds that expected from cosmological expansion, indicating a reduction in number and/or physical size of the absorbing structures with cosmic time. We conclude that a significant fraction of the structures giving rise to H I Lyman limit absorption are in the IGM. These structures are likely cosmologically expanding, leading to a substantial decrease of their H I fraction with time in the otherwise highly reionized IGM. Although our measurements are consistent with previous, more uncertain estimates based on the statistics of Lyman limit systems and (semi)-numerical models (Fig. 11), our inferred redshift evolution of the mean free path is very steep, partly due to our correct accounting for cosmological expansion at low redshifts. The smoothly evolving mean free path tracks the Lyman limit absorption in the highly ionized IGM at  $2.3 < z < 5.5$ , without any obvious indication of a more rapid decrease at the highest redshifts that would signal the approach of the H I reionization epoch. Viable numerical models of H I reionization must nevertheless match the measured post-reionization mean free path and its evolution with redshift (e.g. Gnedin & Fan 2006).

Future work on the mean free path will likely focus on the lowest and highest redshifts. At  $z \sim 1.6$  the mean free path is expected to exceed the horizon of the universe, such that all ionizing sources are expected to contribute to the UV radiation field at any given point (e.g. Madau, Haardt & Rees 1999; O’Meara et al. 2013). Currently, there are efforts to constrain this ‘breakthrough’ epoch with *HST* UV spectroscopy of a sample of  $z_{\text{em}} \sim 1$  quasars (Howk et al. in prep.). At the highest redshifts  $z \gtrsim 6$  the mean free path is expected to drop rapidly, indicating the epoch of H I reionization (e.g. Gnedin 2000). However, measurements of the mean free path are very challenging at  $z \gtrsim 5.5$  due to highly uncertain IGM absorber statistics (Songaila & Cowie 2010) and limitations of the quasar stacking technique (high sky subtraction accuracy required for  $\lambda_{\text{mfp}}^{912} \lesssim 10 \text{ Mpc}$ , uncertainty in the UV SED of quasars, bias due to quasar proximity zones). A direct measurement of the mean free path at  $z > 5.5$  from spectral stacks will require a modest sample of high-quality spectra of either fainter quasars with smaller proximity zones (e.g. Willott et al. 2010) or the brightest  $z \sim 6$  galaxies (e.g. Willott et al. 2013) to be collected with future 30 m telescopes.

## ACKNOWLEDGEMENTS

We thank Francesco Haardt and Piero Madau for useful discussions. Matt McQuinn and Nick Gnedin kindly supplied tabulated mean free path values from their numerical simulations. GW and JXP acknowledge the support from the National Science Foundation (NSF) grant AST-1010004. JXP thanks the Alexander von Humboldt Foundation for a visitor fellowship to the MPIA where part of this work was performed, as well as the MPIA for hospitality during his visits. MTM and JXP thank the Australian Research Council for *Discovery Project* grant DP130100568 which supported this work. JMO thanks the VPAA’s office at Saint Michael’s College for travel support. GDB acknowledges support from the Kavli Foundation and the support of a STFC Ernest Rutherford Fellowship. SL has been supported by FONDECYT grant number

<sup>8</sup> Link to VizieR will be provided upon acceptance of the manuscript.



1100214. BM has been supported by NSF Grant AST-1109665 and the Alfred P. Sloan Foundation.

Based on observations obtained at the Gemini Observatory, which is operated by the Association of Universities for Research in Astronomy, Inc., under a cooperative agreement with the NSF on behalf of the Gemini partnership: the NSF (United States), the National Research Council (Canada), CONICYT (Chile), the Australian Research Council (Australia), Ministério da Ciência, Tecnologia e Inovação (Brazil) and Ministerio de Ciencia, Tecnología e Innovación Productiva (Argentina).

## REFERENCES

- Abazajian K. N. et al., 2009, *ApJS*, 182, 543  
 Abel T., Mo H. J., 1998, *ApJ*, 494, L151+  
 Altay G. et al., 2011, *ApJ*, 737, L37  
 Alvarez M. A., Abel T., 2012, *ApJ*, 747, 126  
 Baldwin J. A., 1977, *ApJ*, 214, 679  
 Beardsley A. P. et al., 2013, *MNRAS*, 429, L5  
 Becker G. D., Bolton J. S., 2013, *MNRAS*, 436, 1023  
 Becker G. D. et al., 2011, *MNRAS*, 410, 1096  
 —, 2013, *MNRAS*, 430, 2067  
 Becker G. D., Rauch M., Sargent W. L. W., 2007, *ApJ*, 662, 72  
 Bèland S., Boulade O., Davidge T., 1988, *Bulletin d'information du telescope Canada-France-Hawaii*, 19, 16  
 Birnboim Y., Dekel A., 2003, *MNRAS*, 345, 349  
 Bolton J. S., Haehnelt M. G., 2007, *MNRAS*, 382, 325  
 Bolton J. S. et al., 2011, *MNRAS*, 416, L70  
 Bouwens R. J. et al., 2012, *ApJ*, 752, L5  
 Calverley A. P. et al., 2011, *MNRAS*, 412, 2543  
 Cardelli J. A., Clayton G. C., Mathis J. S., 1989, *ApJ*, 345, 245  
 Chen H.-W. et al., 2005, *ApJ*, 634, L25  
 Chornock R. et al., 2013, *ApJ*, 774, 26  
 Crociani D. et al., 2011, *MNRAS*, 411, 289  
 Cucchiara A. et al., 2011, *ApJ*, 736, 7  
 Dall'Aglio A., Wisotzki L., Worseck G., 2008, *A&A*, 491, 465  
 Davé R. et al., 2010, *MNRAS*, 408, 2051  
 Dekel A., Birnboim Y., 2006, *MNRAS*, 368, 2  
 Dekel A. et al., 2009, *Nature*, 457, 451  
 Emberson J. D., Thomas R. M., Alvarez M. A., 2013, *ApJ*, 763, 146  
 Fan X. et al., 2006, *AJ*, 132, 117  
 Faucher-Giguère C.-A., Kereš D., 2011, *MNRAS*, 412, L118  
 Faucher-Giguère C.-A. et al., 2008a, *ApJ*, 688, 85  
 —, 2008b, *ApJ*, 673, 39  
 —, 2009, *ApJ*, 703, 1416  
 —, 2008c, *ApJ*, 681, 831  
 Filippenko A. V., 1982, *PASP*, 94, 715  
 Font-Ribera A. et al., 2013, *J. Cosmology Astropart. Phys.*, 5, 18  
 Fumagalli M. et al., 2013a, *ArXiv e-prints*  
 —, 2013b, *ApJ*, 775, 78  
 —, 2011, *MNRAS*, 418, 1796  
 Furlanetto S. R., Oh S. P., 2005, *MNRAS*, 363, 1031  
 Gnedin N. Y., 2000, *ApJ*, 535, 530  
 Gnedin N. Y., Fan X., 2006, *ApJ*, 648, 1  
 Gunn J. E., Peterson B. A., 1965, *ApJ*, 142, 1633  
 Haardt F., Madau P., 2012, *ApJ*, 746, 125  
 Hanuschik R. W., 2003, *A&A*, 407, 1157  
 Hennawi J. F., Prochaska J. X., 2007, *ApJ*, 655, 735  
 Hewett P. C., Wild V., 2010, *MNRAS*, 405, 2302  
 Hook I. M. et al., 2004, *PASP*, 116, 425  
 Kawai N. et al., 2006, *Nature*, 440, 184  
 Kereš D. et al., 2009, *MNRAS*, 395, 160  
 Kim T.-S. et al., 2007, *MNRAS*, 382, 1657  
 —, 2013, *A&A*, 552, A77  
 Kirkman D. et al., 2005, *MNRAS*, 360, 1373  
 Kohler K., Gnedin N. Y., Hamilton A. J. S., 2007, *ApJ*, 657, 15  
 Lidz A. et al., 2010, *ApJ*, 718, 199  
 Madau P., 1995, *ApJ*, 441, 18  
 Madau P., Haardt F., Rees M. J., 1999, *ApJ*, 514, 648  
 McQuinn M., Oh S. P., Faucher-Giguère C.-A., 2011, *ApJ*, 743, 82  
 Meiksin A., 2006, *MNRAS*, 365, 807  
 Meiksin A., Madau P., 1993, *ApJ*, 412, 34  
 Meiksin A., White M., 2004, *MNRAS*, 350, 1107  
 Mesinger A., Furlanetto S., 2009, *MNRAS*, 400, 1461  
 Miralda-Escudé J. et al., 1996, *ApJ*, 471, 582  
 Miralda-Escudé J., Haehnelt M., Rees M. J., 2000, *ApJ*, 530, 1  
 Mortlock D. J. et al., 2011, *Nature*, 474, 616  
 Ocvirk P., Pichon C., Teyssier R., 2008, *MNRAS*, 390, 1326  
 O'Meara J. M. et al., 2013, *ApJ*, 765, 137  
 Pâris I. et al., 2013, *ArXiv e-prints*  
 —, 2011, *A&A*, 530, A50  
 Péroux C. et al., 2003, *MNRAS*, 346, 1103  
 Pober J. C. et al., 2013, *ApJ*, 768, L36  
 Prochaska J. X. et al., 2013, *ApJ*, 776, 136  
 Prochaska J. X., Hennawi J. F., Simcoe R. A., 2013, *ApJ*, 762, L19  
 Prochaska J. X., Herbert-Fort S., Wolfe A. M., 2005, *ApJ*, 635, 123  
 Prochaska J. X. et al., 2014, *MNRAS*, 438, 476  
 Prochaska J. X., O'Meara J. M., Worseck G., 2010, *ApJ*, 718, 392  
 Prochaska J. X., Worseck G., O'Meara J. M., 2009, *ApJ*, 705, L113  
 Rahmati A. et al., 2013, *MNRAS*, 430, 2427  
 Rao S. M., Turnshek D. A., Nestor D. B., 2006, *ApJ*, 636, 610  
 Ribaldo J., Lehner N., Howk J. C., 2011, *ApJ*, 736, 42  
 Richards G. T. et al., 2011, *AJ*, 141, 167  
 —, 2002, *AJ*, 124, 1  
 Rudie G. C. et al., 2013, *ApJ*, 769, 146  
 Schaye J., 2001, *ApJ*, 559, 507  
 Schlegel D. J., Finkbeiner D. P., Davis M., 1998, *ApJ*, 500, 525  
 Schneider D. P. et al., 2010, *AJ*, 139, 2360  
 Scott J. et al., 2000, *ApJS*, 130, 67  
 Shen Y. et al., 2007, *AJ*, 133, 2222  
 Songaila A., 2004, *AJ*, 127, 2598  
 Songaila A., Cowie L. L., 2010, *ApJ*, 721, 1448  
 Stengler-Larrea E. A. et al., 1995, *ApJ*, 444, 64  
 Storrie-Lombardi L. J. et al., 1994, *ApJ*, 427, L13  
 Telfer R. C. et al., 2002, *ApJ*, 565, 773  
 Tytler D., Fan X.-M., 1992, *ApJS*, 79, 1  
 van de Voort F. et al., 2012, *MNRAS*, 421, 2809  
 —, 2011, *MNRAS*, 414, 2458  
 Vanden Berk D. E. et al., 2001, *AJ*, 122, 549  
 White M. et al., 2012, *MNRAS*, 424, 933  
 White R. L. et al., 2003, *AJ*, 126, 1  
 Willott C. J. et al., 2010, *AJ*, 139, 906  
 —, 2013, *AJ*, 145, 4  
 Worseck G., Prochaska J. X., 2011, *ApJ*, 728, 23  
 Yatawatta S. et al., 2013, *A&A*, 550, A136  
 Zaroubi S. et al., 2012, *MNRAS*, 425, 2964

This paper has been typeset from a  $\text{T}_{\text{E}}\text{X}/\text{L}^{\text{A}}\text{T}_{\text{E}}\text{X}$  file prepared by the author.

**APPENDIX A: ONLINE TABLES AND FIGURES**

Table A1. GGG survey.

Quasar	$i$ [mag]	$z_{\text{SDSS}}$	flag*	B600 [Å]	S/N <sup>†</sup>	R400 [Å]
SDSS J001115.23+144601.8	18.28	4.967	0	4910–7830	41	6500–10780
SDSS J004054.65–091526.8	19.20	4.976	3	4950–7870	10	6470–10710
SDSS J010619.24+004823.3	18.61	4.449	0	4340–7240	13	5890–10160
SDSS J012509.42–104300.8	19.43	4.492	0	4340–7240	7	5890–10160
SDSS J021043.16–001818.4	19.17	4.733	0	4630–7550	10	6180–10460
SDSS J023137.65–072854.4	19.55	5.413	0	5130–8060	7	6470–10720
SDSS J033119.66–074143.1	19.12	4.739	0	4630–7550	10	6180–10460
SDSS J033829.30+002156.2	20.07	5.032	2	4950–7870	7	6480–10720
SDSS J073103.12+445949.4	19.23	5.004	0	4910–7830	27	6490–10780
SDSS J075907.57+180054.7	19.18	4.862	1	4620–7530	13	6490–10780
SDSS J080023.01+305101.1	19.06	4.685	0	4620–7530	19	6190–10470
SDSS J080715.11+132805.1	19.43	4.875	0	4620–7530	17	6490–10780
SDSS J081806.87+071920.2	18.61	4.581	0	4630–7560	11	6180–10460
SDSS J082212.34+160436.9	19.05	4.488	0	4340–7240	10	5890–10170
SDSS J082454.02+130217.0	20.00	5.188	0	5110–8030	13	6490–10780
SDSS J083655.80+064104.6	19.04	4.436	0	4340–7240	7	5890–10160
SDSS J083920.53+352459.3	19.54	4.777	0	4620–7530	7	6190–10470
SDSS J084627.84+080051.7	19.84	5.030	0	4950–7870	7	6470–10720
SDSS J084631.52+241108.3	19.22	4.743	0	4620–7530	11	6190–10470
SDSS J085430.37+205650.8	19.43	5.179	0	5110–8030	8	6490–10780
SDSS J085707.94+321031.9	18.73	4.776	0	4620–7530	23	6190–10470
SDSS J090100.61+472536.2	19.53	4.608	0	4620–7530	15	6200–10470
SDSS J090245.76+085115.8	20.15	5.226	0	5140–8060	7	6480–10720
SDSS J090634.84+023433.8	18.50	4.511	0	4340–7240	10	5890–10160
SDSS J091316.55+591921.6	20.48	5.122	0	5110–8030	7	6490–10770
SDSS J091543.63+492416.6	19.54	5.196	6	5110–8030	16	6500–10780
SDSS J092216.81+265358.9	20.24	5.032	0	4910–7830	7	6490–10770
SDSS J093523.31+411518.5	19.58	4.787	0	4620–7530	17	6190–10470
SDSS J094056.01+584830.2	19.32	4.659	0	4620–7530	19	6190–10470
SDSS J094108.36+594725.7	19.30	4.790	0	4620–7530	15	6190–10470
SDSS J094409.52+100656.6	19.30	4.748	0	4630–7560	10	6180–10460
SDSS J095632.03+321612.6	19.24	4.647	0	4620–7530	21	6190–10470
SDSS J095707.67+061059.5	19.27	5.185	0	5140–8060	7	6470–10720
SDSS J100251.20+223135.1	19.40	4.744	0	4620–7530	12	6190–10470
SDSS J100416.12+434739.0	19.39	4.872	0	4620–7530	10	6490–10780
SDSS J100444.30+202520.0	20.24	5.084	1	4910–7830	12	6490–10780
SDSS J101549.00+002020.0	19.28	4.403	0	4340–7240	10	5890–10160
SDSS J102332.07+633508.0	19.69	4.881	6	4910–7830	13	6490–10770
SDSS J102622.87+471907.2	18.74	4.943	0	4910–7830	20	6490–10780
SDSS J102623.61+254259.5	20.04	5.303	0	5110–8030	7	6500–10780
SDSS J103418.65+203300.2	19.79	4.998	2	4910–7830	18	6490–10780
SDSS J103601.03+500831.7	19.23	4.470	1	4320–7220	27	5890–10160
SDSS J103711.04+313433.5	19.52	4.885	0	4910–7830	16	6490–10780
SDSS J103919.28+344504.5	19.33	4.420	0	4320–7230	20	5890–10160
SDSS J104041.09+162233.8	18.96	4.814	0	4910–7830	13	6490–10780
SDSS J104325.55+404849.5	19.09	4.934	6	4910–7830	10	6490–10780
SDSS J104351.19+650647.6	19.10	4.471	0	4320–7220	20	5890–10160
SDSS J105020.40+262002.3	19.47	4.796	0	4620–7530	10	6190–10470
SDSS J105036.46+580424.6	19.66	5.132	0	5110–8030	7	6490–10780
SDSS J105322.98+580412.1	19.81	5.215	0	5110–8030	9	6490–10780
SDSS J105445.43+163337.4	20.22	5.187	6	5110–8030	7	6490–10780
SDSS J110045.23+112239.1	18.85	4.707	0	4630–7560	7	6180–10460
SDSS J110134.36+053133.8	19.25	4.987	4	4950–7870	7	6470–10720
SDSS J111523.24+082918.4	19.56	4.640	2	4620–7550	7	6180–10460
SDSS J111741.26+261039.2	19.52	4.635	0	4620–7530	21	6200–10470
SDSS J111920.64+345248.1	20.05	5.011	0	4910–7830	10	6490–10780
SDSS J112253.50+005329.7	19.10	4.551	0	4630–7560	15	6190–10460
SDSS J112534.93+380149.3	19.50	4.618	0	4620–7530	15	6200–10470
SDSS J112857.84+575909.8	19.49	4.978	0	4910–7830	11	6490–10770
SDSS J113246.50+120901.6	19.76	5.167	0	5130–8060	7	6470–10710
SDSS J114008.67+620530.0	19.24	4.521	0	4320–7230	18	5890–10160
SDSS J114225.30+110217.3	19.39	4.590	0	4630–7560	10	6180–10460
SDSS J114657.79+403708.6	19.41	5.005	0	4910–7830	13	6490–10780
SDSS J114826.16+302019.3	20.06	5.142	0	5110–8030	10	6490–10780
SDSS J114914.88+281308.7	18.52	4.553	0	4620–7530	38	6200–10470

**Table A1** – *continued* GGG survey.

Quasar	$i$ [mag]	$z_{\text{SDSS}}$	flag*	B600 [Å]	S/N <sup>†</sup>	R400 [Å]
SDSS J115424.73+134145.7	20.18	5.010	4	4950–7870	7	6470–10720
SDSS J115809.39+634252.8	19.34	4.494	0	4320–7230	20	5890–10160
SDSS J120036.72+461850.2	19.28	4.730	0	4620–7530	11	6190–10470
SDSS J120055.61+181732.9	19.67	4.984	0	4950–7870	7	6470–10710
SDSS J120102.01+073648.1	19.43	4.443	7	4340–7250	10	5890–10160
SDSS J120110.31+211758.5	18.73	4.579	6	4620–7530	20	6200–10470
SDSS J120131.56+053510.1	19.48	4.830	1	4630–7560	10	6470–10720
SDSS J120207.78+323538.8	19.27	5.292	0	5110–8030	7	6490–10770
SDSS J120441.73–002149.6	19.28	5.032	0	4950–7870	7	6470–10710
SDSS J120725.27+321530.4	19.15	4.643	0	4620–7530	16	6200–10470
SDSS J120730.84+153338.1	18.99	4.465	0	4330–7240	12	5890–10160
SDSS J120952.72+183147.2	19.86	5.158	0	5140–8060	5	6470–10720
SDSS J121134.04+484235.9	19.23	4.505	0	4320–7220	17	5890–10160
SDSS J121422.02+665707.5	18.88	4.639	1	4620–7530	7	6200–10470
SDSS J122016.05+315253.0	19.08	4.891	0	4910–7830	24	6490–10780
SDSS J122146.42+444528.0	19.96	5.206	0	5110–8030	7	6490–10780
SDSS J122237.96+195842.9	20.06	5.189	2	5140–8060	5	6470–10710
SDSS J123333.47+062234.2	20.06	5.289	0	5140–8060	7	6470–10710
SDSS J124247.91+521306.8	20.01	5.018	0	4910–7830	10	6490–10780
SDSS J124400.04+553406.8	19.59	4.625	1	4620–7530	7	6200–10470
SDSS J124515.46+382247.5	19.66	4.933	6	4910–7830	16	6490–10770
SDSS J125025.40+183458.1	19.34	4.599	5	4630–7560	13	6180–10460
SDSS J125353.35+104603.1	19.42	4.909	0	4950–7870	14	6470–10710
SDSS J125718.02+374729.9	19.23	4.750	0	4620–7530	19	6190–10470
SDSS J130002.16+011823.0	18.81	4.613	0	4630–7560	13	6190–10470
SDSS J130110.95+252738.3	19.41	4.660	0	4620–7530	17	6190–10470
SDSS J130152.55+221012.1	19.67	4.829	6	4620–7530	20	6490–10780
SDSS J130215.71+550553.5	19.03	4.436	0	4320–7230	20	5890–10160
SDSS J130619.38+023658.9	19.67	4.837	4	4630–7560	7	6470–10710
SDSS J130917.12+165758.5	18.94	4.692	0	4630–7560	7	6180–10460
SDSS J131234.08+230716.3	19.38	4.996	1	4910–7830	10	6490–10770
SDSS J132512.49+112329.7	19.18	4.412	0	4330–7240	11	5890–10160
SDSS J133203.86+553105.0	19.23	4.734	0	4620–7530	17	6190–10470
SDSS J133250.08+465108.6	19.62	4.855	0	4620–7530	9	6490–10770
SDSS J133412.56+122020.7	19.94	5.134	0	5140–8060	7	6480–10720
SDSS J133728.81+415539.8	19.55	5.015	0	4910–7830	10	6490–10780
SDSS J134015.03+392630.7	19.53	5.026	0	4910–7830	16	6490–10780
SDSS J134040.24+281328.1	20.05	5.338	0	5110–8030	7	6490–10770
SDSS J134134.19+014157.7	18.91	4.670	0	4630–7560	10	6190–10470
SDSS J134141.45+461110.3	20.22	5.023	0	4910–7830	7	6490–10780
SDSS J134154.01+351005.6	19.71	5.267	0	5110–8030	10	6490–10780
SDSS J134743.29+495621.3	17.62	4.510	0	4320–7230	20	5890–10160
SDSS J134819.87+181925.8	19.21	4.961	6	4950–7870	10	6470–10720
SDSS J140146.53+024434.7	18.59	4.441	6	4340–7250	27	5890–10160
SDSS J140404.63+031403.9	19.53	4.870	4	4630–7560	7	6470–10720
SDSS J140503.29+334149.8	18.83	4.459	4	4320–7220	19	5890–10160
SDSS J141209.96+062406.9	19.45	4.467	3	4330–7240	10	5890–10170
SDSS J141914.18–015012.6	19.07	4.586	1	4630–7560	7	6190–10470
SDSS J142025.75+615510.0	19.17	4.434	0	4320–7230	17	5890–10160
SDSS J142144.98+351315.4	18.96	4.556	5	4620–7530	10	6190–10470
SDSS J142325.92+130300.6	19.71	5.037	0	4950–7870	7	6470–10720
SDSS J142526.09+082718.4	18.81	4.945	0	4950–7870	10	6470–10710
SDSS J142705.86+330817.9	18.90	4.718	0	4620–7530	20	6200–10470
SDSS J143352.21+022713.9	18.34	4.721	4	4630–7560	10	6180–10460
SDSS J143605.00+213239.2	20.01	5.250	0	5110–8030	12	6500–10780
SDSS J143629.94+063508.0	19.65	4.851	0	4630–7560	7	6470–10720
SDSS J143751.82+232313.3	19.52	5.317	0	5110–8030	10	6490–10770
SDSS J143835.95+431459.2	17.64	4.611	0	4620–7530	25	6200–10470
SDSS J143850.48+055622.6	19.30	4.437	3	4330–7240	20	5890–10170
SDSS J144331.17+272436.7	19.02	4.443	6	4320–7230	35	5890–10160
SDSS J144407.63–010152.7	19.30	4.518	0	4330–7240	10	5890–10170
SDSS J144717.97+040112.4	19.17	4.580	1	4630–7560	7	6190–10470
SDSS J145107.93+025615.6	19.19	4.481	0	4330–7240	10	5890–10170
SDSS J150027.89+434200.8	19.01	4.643	0	4620–7530	18	6200–10470
SDSS J150802.28+430645.4	19.09	4.694	0	4620–7530	17	6190–10470

Table A1 – continued GGG survey.

Quasar	$i$ [mag]	$z_{\text{SDSS}}$	flag*	B600 [Å]	S/N <sup>†</sup>	R400 [Å]
SDSS J151155.98+040802.9	19.57	4.686	0	4630–7560	10	6190–10460
SDSS J151320.89+105807.3	19.39	4.618	4	4620–7550	13	6210–10490
SDSS J151719.09+490003.2	19.57	4.681	0	4620–7530	14	6200–10470
SDSS J152005.93+233953.0	19.16	4.484	0	4320–7230	20	5890–10160
SDSS J152404.23+134417.5	19.50	4.810	0	4630–7560	7	6470–10720
SDSS J153247.41+223704.1	18.32	4.417	0	4320–7230	20	5890–10160
SDSS J153459.75+132701.4	19.88	5.059	0	4910–7840	7	6470–10710
SDSS J153650.25+500810.3	18.52	4.927	0	4910–7830	33	6490–10780
SDSS J154352.92+333759.5	19.58	4.602	0	4610–7530	13	6190–10470
SDSS J155243.04+255229.2	19.58	4.667	2	4620–7530	10	6200–10470
SDSS J155426.16+193703.0	18.00	4.612	0	4630–7560	26	6180–10460
SDSS J160336.64+350824.3	18.55	4.460	4	4320–7220	32	5890–10160
SDSS J160516.16+210638.5	19.01	4.475	0	4320–7230	10	5890–10160
SDSS J160734.22+160417.4	19.24	4.798	0	4630–7560	10	6180–10460
SDSS J161105.64+084435.4	18.91	4.545	0	4330–7240	21	5890–10160
SDSS J161425.13+464028.9	20.11	5.313	0	5110–8030	7	6490–10770
SDSS J161447.03+205902.9	20.03	5.091	0	4910–7830	9	6490–10770
SDSS J161616.26+513336.9	19.47	4.536	0	4320–7230	21	5890–10160
SDSS J161622.10+050127.7	18.83	4.872	0	4630–7550	11	6470–10720
SDSS J162445.03+271418.7	18.68	4.496	0	4320–7230	29	5890–10160
SDSS J162626.50+275132.4	19.30	5.275	0	5110–8030	10	6490–10780
SDSS J162629.19+285857.5	19.94	5.022	0	4910–7830	5	6490–10780
SDSS J163411.82+215325.0	19.03	4.529	3	4320–7230	20	5890–10160
SDSS J163636.93+315717.1	18.61	4.559	0	4620–7530	17	6200–10470
SDSS J165902.12+270935.1	19.50	5.312	0	5110–8030	7	6490–10770
SDSS J173744.87+582829.6	19.34	4.916	2	4910–7830	14	6490–10780
SDSS J205724.14–003018.7	18.70	4.663	0	4630–7560	11	6180–10460
SDSS J214725.71–083834.6	18.32	4.588	0	4630–7560	12	6190–10470
SDSS J220008.66+001744.9	19.15	4.817	0	4630–7560	11	6470–10720
SDSS J222509.19–001406.9	19.34	4.885	0	4950–7870	12	6470–10720
SDSS J222845.14–075755.3	19.88	5.142	0	5130–8060	7	6470–10720
SDSS J225246.43+142525.8	19.80	4.904	0	4620–7550	10	6480–10720
SDSS J234003.51+140257.1	18.98	4.559	0	4620–7550	10	6220–10500

\*Flag describing quasar spectrum: (1) BAL; (2) associated absorption; (3) weak-lined QSO; (4) candidate weak-lined QSO; (5) PDLA; (6) PLLS; (7) contaminated by neighbour.

†Signal-to-Noise ratio per 2.76 Å pixel at rest-frame wavelength 1450 Å (R400).

**Table A2.** GGG Quasar emission redshifts.

Quasar	$z_{\text{SDSS}}$	$z_{\text{GGG}}$	Shen Lines	$z_{\text{Shen}}$	$z_{\text{HW}}$
SDSS J001115.23+144601.8	4.967	4.970 ± 0.005	Si IV, C IV	4.959 ± 0.014	4.974
SDSS J004054.65−091526.8	4.976	4.980 ± 0.010	Si IV	4.981 ± 0.016	4.977
SDSS J010619.24+004823.3	4.449	4.449 ± 0.005	Si IV, C IV	4.434 ± 0.013	4.450
SDSS J012509.42−104300.8	4.492	4.498 ± 0.005	Si IV, C IV	4.500 ± 0.013	4.503
SDSS J021043.16−001818.4	4.733	4.770 ± 0.020	Si IV, C IV	4.746 ± 0.014	4.708
SDSS J023137.65−072854.4	5.413	5.420 ± 0.005	Si IV, C IV	5.418 ± 0.015	5.415
SDSS J033119.66−074143.1	4.739	4.734 ± 0.010	Si IV, C IV	4.734 ± 0.014	4.733
SDSS J033829.30+002156.2	5.032	5.040 ± 0.020	Si IV, C IV	5.030 ± 0.014	5.033
SDSS J073103.12+445949.4	5.004	4.998 ± 0.005	Si IV, C IV	4.988 ± 0.014	5.009
SDSS J075907.57+180054.7	4.862	4.820 ± 0.010	Si IV, C IV	4.798 ± 0.014	4.815
SDSS J080023.01+305101.1	4.685	4.676 ± 0.005	Si IV, C IV	4.690 ± 0.014	4.689
SDSS J080715.11+132805.1	4.875	4.880 ± 0.010	Si IV, C IV	4.858 ± 0.014	4.872
SDSS J081806.87+071920.2	4.581	4.625 ± 0.010	Si IV	4.580 ± 0.015	4.616
SDSS J082212.34+160436.9	4.488	4.510 ± 0.020	C IV	4.502 ± 0.015	4.481
SDSS J082454.02+130217.0	5.188	5.207 ± 0.005	Si IV, C IV	5.193 ± 0.015	...
SDSS J083655.80+064104.6	4.436	4.435 ± 0.010	Si IV, C IV	4.401 ± 0.013	4.416
SDSS J083920.53+352459.3	4.777	4.784 ± 0.010	Si IV	4.790 ± 0.015	4.794
SDSS J084627.84+080051.7	5.030	5.028 ± 0.010	Si IV	5.047 ± 0.016	5.031
SDSS J084631.52+241108.3	4.743	4.742 ± 0.005	Si IV, C IV	4.710 ± 0.014	4.722
SDSS J085430.37+205650.8	5.179	5.179 ± 0.005	Si IV, C IV	5.177 ± 0.015	5.191
SDSS J085707.94+321031.9	4.776	4.796 ± 0.010	Si IV, C IV	4.783 ± 0.014	4.799
SDSS J090100.61+472536.2	4.608	4.598 ± 0.010	Si IV, C IV	4.593 ± 0.013	4.606
SDSS J090245.76+085115.8	5.226	5.226 ± 0.010	C IV	5.267 ± 0.017	5.227
SDSS J090634.84+023433.8	4.511	4.516 ± 0.005	Si IV, C IV	4.521 ± 0.013	4.504
SDSS J091316.55+591921.6	5.122	5.122 ± 0.005	Si IV, C IV	5.121 ± 0.015	5.122
SDSS J091543.63+492416.6	5.196	5.199 ± 0.005	Si IV, C IV	5.210 ± 0.015	5.197
SDSS J092216.81+265358.9	5.032	5.042 ± 0.010	Si IV, C IV	5.041 ± 0.014	5.033
SDSS J093523.31+411518.5	4.787	4.806 ± 0.010	Si IV, C IV	4.763 ± 0.014	4.782
SDSS J094056.01+584830.2	4.659	4.664 ± 0.005	Si IV, C IV	4.656 ± 0.013	4.658
SDSS J094108.36+594725.7	4.790	4.852 ± 0.005	Si IV, C IV	4.850 ± 0.014	4.861
SDSS J094409.52+100656.6	4.748	4.776 ± 0.005	Si IV, C IV	4.767 ± 0.014	4.773
SDSS J095632.03+321612.6	4.647	4.632 ± 0.005	Si IV, C IV	4.601 ± 0.013	4.618
SDSS J095707.67+061059.5	5.185	5.167 ± 0.005	Si IV, C IV	5.145 ± 0.015	5.180
SDSS J100251.20+223135.1	4.744	4.761 ± 0.005	Si IV, C IV	4.758 ± 0.014	4.755
SDSS J100416.12+434739.0	4.872	4.872 ± 0.010	Si IV, C IV	4.853 ± 0.014	4.879
SDSS J100444.30+202520.0	5.084	5.084 ± 0.020	C IV	5.089 ± 0.016	5.085
SDSS J101549.00+002020.0	4.403	4.406 ± 0.005	Si IV, C IV	4.406 ± 0.013	4.416
SDSS J102332.07+633508.0	4.881	4.872 ± 0.010	Si IV, C IV	4.864 ± 0.014	4.882
SDSS J102622.87+471907.2	4.943	4.932 ± 0.010	Si IV, C IV	4.928 ± 0.014	4.948
SDSS J102623.61+254259.5	5.303	5.254 ± 0.020	Si IV, C IV	5.263 ± 0.015	5.285
SDSS J103418.65+203300.2	4.998	4.998 ± 0.005	Si IV, C IV	4.994 ± 0.014	4.999
SDSS J103601.03+500831.7	4.470	4.480 ± 0.020	Si IV	4.528 ± 0.015	4.529
SDSS J103711.04+313433.5	4.885	4.916 ± 0.010	Si IV, C IV	4.881 ± 0.014	4.873
SDSS J103919.28+344504.5	4.420	4.421 ± 0.005	Si IV, C IV	4.409 ± 0.013	4.410
SDSS J104041.09+162233.8	4.814	4.809 ± 0.010	Si IV, C IV	4.822 ± 0.014	...
SDSS J104325.55+404849.5	4.934	4.923 ± 0.005	Si IV, C IV	4.921 ± 0.014	4.930
SDSS J104351.19+650647.6	4.471	4.516 ± 0.010	C IV	4.481 ± 0.015	4.482
SDSS J105020.40+262002.3	4.796	4.892 ± 0.010	Si IV, C IV	4.807 ± 0.014	4.838
SDSS J105036.46+580424.6	5.132	5.151 ± 0.005	Si IV, C IV	5.174 ± 0.015	5.133
SDSS J105322.98+580412.1	5.215	5.250 ± 0.020	Si IV, C IV	5.240 ± 0.015	5.260
SDSS J105445.43+163337.4	5.187	5.154 ± 0.005	Si IV, C IV	5.129 ± 0.015	5.148
SDSS J110045.23+112239.1	4.707	4.728 ± 0.010	Si IV, C IV	4.736 ± 0.014	4.734
SDSS J110134.36+053133.8	4.987	5.045 ± 0.020	Si IV, C IV	4.930 ± 0.014	4.998
SDSS J111523.24+082918.4	4.640	4.710 ± 0.030	Si IV, C IV	4.684 ± 0.014	4.641
SDSS J111741.26+261039.2	4.635	4.626 ± 0.010	Si IV, C IV	4.626 ± 0.013	4.641
SDSS J111920.64+345248.1	5.011	4.992 ± 0.005	Si IV, C IV	4.981 ± 0.014	5.012
SDSS J112253.50+005329.7	4.551	4.586 ± 0.005	Si IV, C IV	4.578 ± 0.013	4.584
SDSS J112534.93+380149.3	4.618	4.606 ± 0.010	Si IV, C IV	4.581 ± 0.013	4.588
SDSS J112857.84+575909.8	4.978	4.992 ± 0.020	Si IV, C IV	4.973 ± 0.014	5.000
SDSS J113246.50+120901.6	5.167	5.180 ± 0.005	Si IV	5.118 ± 0.016	5.168
SDSS J114008.67+620530.0	4.521	4.523 ± 0.005	Si IV, C IV	4.522 ± 0.013	4.530
SDSS J114225.30+110217.3	4.590	4.596 ± 0.005	Si IV, C IV	4.588 ± 0.013	4.590
SDSS J114657.79+403708.6	5.005	4.996 ± 0.010	Si IV, C IV	4.988 ± 0.014	5.006
SDSS J114826.16+302019.3	5.142	5.128 ± 0.005	Si IV, C IV	5.104 ± 0.015	5.143
SDSS J114914.88+281308.7	4.553	4.556 ± 0.005	Si IV, C IV	4.548 ± 0.013	4.554

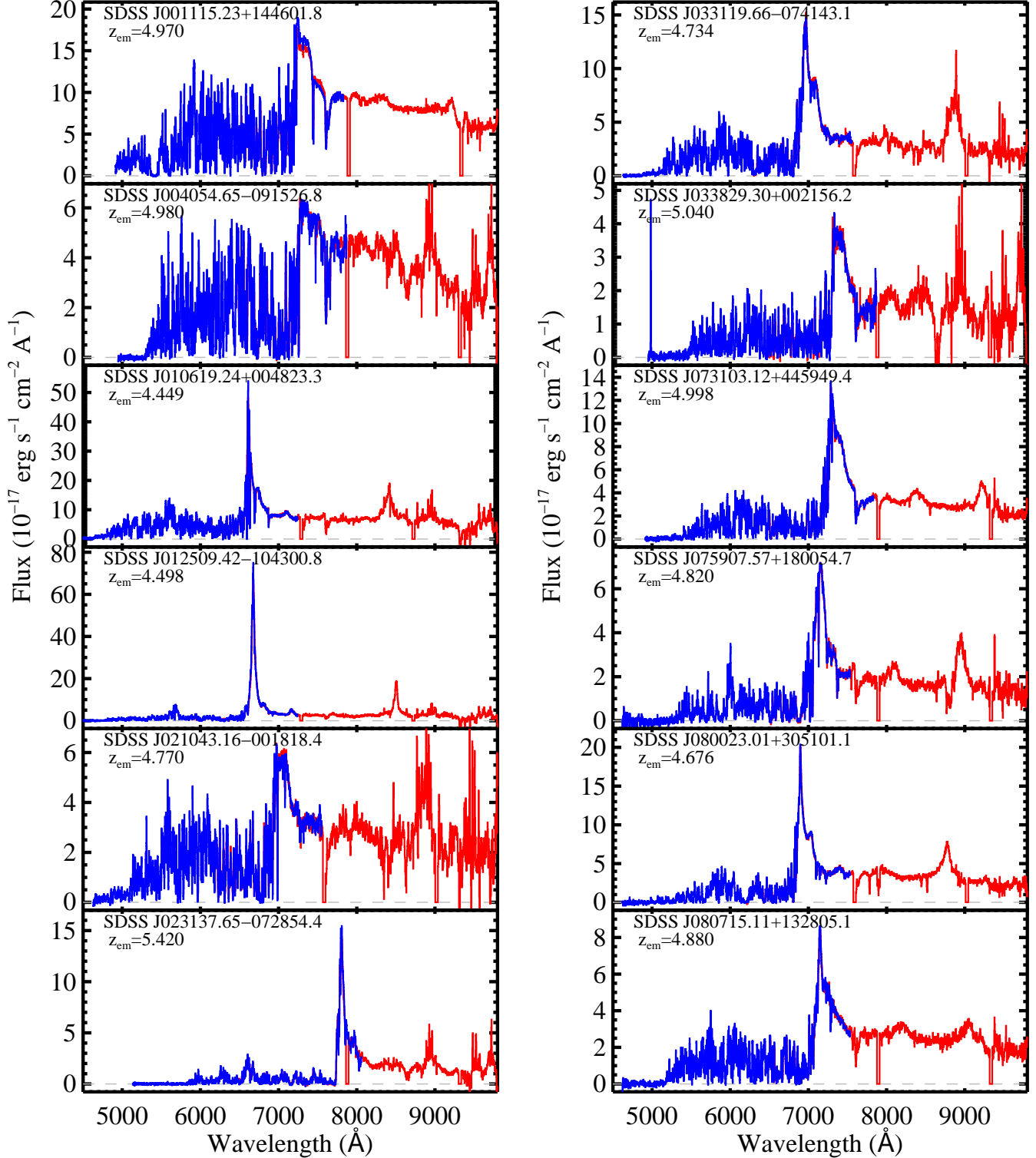


Table A2 – continued GGG Quasar emission redshifts.

Quasar	$z_{\text{SDSS}}$	$z_{\text{GGG}}$	Shen Lines	$z_{\text{Shen}}$	$z_{\text{HW}}$
SDSS J115424.73+134145.7	5.010	5.060 ± 0.020	Si IV	5.005 ± 0.016	5.011
SDSS J115809.39+634252.8	4.494	4.479 ± 0.010	Si IV, CIV	4.439 ± 0.013	4.444
SDSS J120036.72+461850.2	4.730	4.741 ± 0.010	Si IV, CIV	4.752 ± 0.014	4.754
SDSS J120055.61+181732.9	4.984	4.995 ± 0.020	Si IV, CIV	4.998 ± 0.014	...
SDSS J120102.01+073648.1	4.443	4.472 ± 0.005	CIV	4.454 ± 0.014	4.460
SDSS J120110.31+211758.5	4.579	4.579 ± 0.005	Si IV, CIV	4.564 ± 0.013	...
SDSS J120131.56+053510.1	4.830	4.840 ± 0.020	Si IV, CIV	4.744 ± 0.014	4.831
SDSS J120207.78+323538.8	5.292	5.298 ± 0.005	Si IV, CIV	5.256 ± 0.015	5.275
SDSS J120441.73-002149.6	5.032	5.094 ± 0.010	Si IV	5.108 ± 0.016	5.033
SDSS J120725.27+321530.4	4.643	4.621 ± 0.005	Si IV, CIV	4.614 ± 0.013	4.609
SDSS J120730.84+153338.1	4.465	4.452 ± 0.010	CIV	4.456 ± 0.014	4.450
SDSS J120952.72+183147.2	5.158	5.127 ± 0.005	CIV	5.157 ± 0.016	...
SDSS J121134.04+484235.9	4.505	4.544 ± 0.005	Si IV, CIV	4.518 ± 0.013	4.508
SDSS J121422.02+665707.5	4.639	4.650 ± 0.020	Si IV, CIV	4.626 ± 0.013	4.650
SDSS J122016.05+315253.0	4.891	4.900 ± 0.010	Si IV, CIV	4.847 ± 0.014	4.861
SDSS J122146.42+444528.0	5.206	5.203 ± 0.005	Si IV, CIV	5.201 ± 0.015	5.207
SDSS J122237.96+195842.9	5.189	5.120 ± 0.020	Si IV, CIV	5.119 ± 0.015	...
SDSS J123333.47+062234.2	5.289	5.300 ± 0.020	Si IV, CIV	5.339 ± 0.015	5.290
SDSS J124247.91+521306.8	5.018	5.036 ± 0.005	Si IV, CIV	5.054 ± 0.014	5.018
SDSS J124400.04+553406.8	4.625	4.660 ± 0.020	Si IV	4.628 ± 0.015	4.637
SDSS J124515.46+382247.5	4.933	4.963 ± 0.010	Si IV, CIV	4.962 ± 0.014	4.934
SDSS J125025.40+183458.1	4.599	4.557 ± 0.005	Si IV, CIV	4.543 ± 0.013	...
SDSS J125353.35+104603.1	4.909	4.918 ± 0.005	Si IV	4.915 ± 0.016	...
SDSS J125718.02+374729.9	4.750	4.733 ± 0.010	Si IV, CIV	4.728 ± 0.014	4.741
SDSS J130002.16+011823.0	4.613	4.619 ± 0.005	Si IV, CIV	4.603 ± 0.013	4.601
SDSS J130110.95+252738.3	4.660	4.666 ± 0.005	Si IV, CIV	4.664 ± 0.013	...
SDSS J130152.55+221012.1	4.829	4.805 ± 0.020	Si IV, CIV	4.758 ± 0.014	...
SDSS J130215.71+550553.5	4.436	4.461 ± 0.010	Si IV, CIV	4.444 ± 0.013	4.454
SDSS J130619.38+023658.9	4.837	4.860 ± 0.020	Si IV, CIV	4.760 ± 0.014	4.802
SDSS J130917.12+165758.5	4.692	4.714 ± 0.010	Si IV, CIV	4.720 ± 0.014	...
SDSS J131234.08+230716.3	4.996	4.960 ± 0.020	Si IV, CIV	4.952 ± 0.014	...
SDSS J132512.49+112329.7	4.412	4.412 ± 0.005	Si IV, CIV	4.416 ± 0.013	4.415
SDSS J133203.86+553105.0	4.734	4.737 ± 0.005	Si IV, CIV	4.739 ± 0.014	4.748
SDSS J133250.08+465108.6	4.855	4.844 ± 0.010	Si IV, CIV	4.857 ± 0.014	4.867
SDSS J133412.56+122020.7	5.134	5.130 ± 0.010	Si IV	5.093 ± 0.016	5.135
SDSS J133728.81+415539.8	5.015	5.018 ± 0.010	Si IV, CIV	5.021 ± 0.014	5.016
SDSS J134015.03+392630.7	5.026	5.048 ± 0.010	Si IV, CIV	5.041 ± 0.014	5.052
SDSS J134040.24+281328.1	5.338	5.349 ± 0.005	Si IV, CIV	5.339 ± 0.015	5.339
SDSS J134134.19+014157.7	4.670	4.696 ± 0.010	Si IV, CIV	4.701 ± 0.014	4.677
SDSS J134141.45+461110.3	5.023	5.003 ± 0.005	Si IV, CIV	5.008 ± 0.014	4.998
SDSS J134154.01+351005.6	5.267	5.252 ± 0.005	Si IV, CIV	5.245 ± 0.015	5.253
SDSS J134743.29+495621.3	4.510	4.563 ± 0.005	Si IV, CIV	4.536 ± 0.013	4.538
SDSS J134819.87+181925.8	4.961	4.954 ± 0.005	Si IV, CIV	4.941 ± 0.014	...
SDSS J140146.53+024434.7	4.441	4.415 ± 0.020	Si IV, CIV	4.412 ± 0.013	4.409
SDSS J140404.63+031403.9	4.870	4.924 ± 0.020	Si IV, CIV	4.783 ± 0.014	4.871
SDSS J140503.29+334149.8	4.459	4.467 ± 0.010	CIV	4.485 ± 0.015	4.460
SDSS J141209.96+062406.9	4.467	4.411 ± 0.010	CIV	4.513 ± 0.015	4.467
SDSS J141914.18-015012.6	4.586	4.590 ± 0.020	Si IV, CIV	4.545 ± 0.013	4.571
SDSS J142025.75+615510.0	4.434	4.448 ± 0.005	CIV	4.447 ± 0.014	4.452
SDSS J142144.98+351315.4	4.556	4.599 ± 0.005	Si IV, CIV	4.564 ± 0.013	4.561
SDSS J142325.92+130300.6	5.037	5.048 ± 0.010	Si IV	5.074 ± 0.016	5.030
SDSS J142526.09+082718.4	4.945	4.955 ± 0.005	Si IV, CIV	4.968 ± 0.014	4.970
SDSS J142705.86+330817.9	4.718	4.703 ± 0.005	Si IV, CIV	4.694 ± 0.014	4.708
SDSS J143352.21+022713.9	4.721	4.729 ± 0.010	Si IV, CIV	4.730 ± 0.014	4.685
SDSS J143605.00+213239.2	5.250	5.227 ± 0.005	Si IV, CIV	5.233 ± 0.015	...
SDSS J143629.94+063508.0	4.851	4.828 ± 0.005	Si IV	5.094 ± 0.016	4.816
SDSS J143751.82+232313.3	5.317	5.320 ± 0.005	Si IV, CIV	5.316 ± 0.015	5.333
SDSS J143835.95+431459.2	4.611	4.686 ± 0.010	Si IV, CIV	4.653 ± 0.013	4.674
SDSS J143850.48+055622.6	4.437	4.437 ± 0.010	CIV	4.506 ± 0.015	4.428
SDSS J144331.17+272436.7	4.443	4.424 ± 0.010	Si IV, CIV	4.410 ± 0.013	...
SDSS J144407.63-010152.7	4.518	4.530 ± 0.005	Si IV, CIV	4.514 ± 0.013	4.521
SDSS J144717.97+040112.4	4.580	4.580 ± 0.020	Si IV, CIV	4.514 ± 0.013	4.584
SDSS J145107.93+025615.6	4.481	4.483 ± 0.005	CIV	4.483 ± 0.015	4.482
SDSS J150027.89+434200.8	4.643	4.641 ± 0.005	Si IV, CIV	4.619 ± 0.013	4.639
SDSS J150802.28+430645.4	4.694	4.681 ± 0.010	Si IV, CIV	4.680 ± 0.014	4.683

**Table A2** – *continued* GGG Quasar emission redshifts.

Quasar	$z_{\text{SDSS}}$	$z_{\text{GGG}}$	Shen Lines	$z_{\text{Shen}}$	$z_{\text{HW}}$
SDSS J151155.98+040802.9	4.686	$4.679 \pm 0.005$	Si IV, C IV	$4.689 \pm 0.014$	4.674
SDSS J151320.89+105807.3	4.618	$4.625 \pm 0.020$	Si IV, C IV	$4.607 \pm 0.013$	4.618
SDSS J151719.09+490003.2	4.681	$4.660 \pm 0.010$	Si IV, C IV	$4.649 \pm 0.013$	4.652
SDSS J152005.93+233953.0	4.484	$4.487 \pm 0.005$	Ly $\alpha$	$4.467 \pm 0.027$	...
SDSS J152404.23+134417.5	4.810	$4.788 \pm 0.010$	Si IV, C IV	$4.786 \pm 0.014$	...
SDSS J153247.41+223704.1	4.417	$4.434 \pm 0.005$	Si IV, C IV	$4.412 \pm 0.013$	...
SDSS J153459.75+132701.4	5.059	$5.043 \pm 0.010$	Si IV, C IV	$5.072 \pm 0.014$	...
SDSS J153650.25+500810.3	4.927	$4.929 \pm 0.005$	Si IV	$4.926 \pm 0.016$	4.941
SDSS J154352.92+333759.5	4.602	$4.604 \pm 0.005$	Si IV, C IV	$4.589 \pm 0.013$	4.594
SDSS J155243.04+255229.2	4.667	$4.645 \pm 0.010$	Si IV, C IV	$4.652 \pm 0.013$	4.667
SDSS J155426.16+193703.0	4.612	$4.632 \pm 0.005$	Si IV, C IV	$4.566 \pm 0.013$	...
SDSS J160336.64+350824.3	4.460	$4.485 \pm 0.010$	Si IV, C IV	$4.429 \pm 0.013$	4.405
SDSS J160516.16+210638.5	4.475	$4.495 \pm 0.010$	Si IV, C IV	$4.491 \pm 0.013$	4.496
SDSS J160734.22+160417.4	4.798	$4.786 \pm 0.010$	Si IV, C IV	$4.772 \pm 0.014$	4.783
SDSS J161105.64+084435.4	4.545	$4.545 \pm 0.005$	Si IV, C IV	$4.561 \pm 0.013$	4.551
SDSS J161425.13+464028.9	5.313	$5.313 \pm 0.005$	Si IV, C IV	$5.320 \pm 0.015$	5.316
SDSS J161447.03+205902.9	5.091	$5.081 \pm 0.020$	Si IV, C IV	$5.025 \pm 0.014$	5.092
SDSS J161616.26+513336.9	4.536	$4.528 \pm 0.005$	Si IV	$4.523 \pm 0.015$	4.530
SDSS J161622.10+050127.7	4.872	$4.876 \pm 0.010$	Si IV, C IV	$4.794 \pm 0.014$	4.863
SDSS J162445.03+271418.7	4.496	$4.498 \pm 0.005$	C IV	$4.451 \pm 0.014$	4.476
SDSS J162626.50+275132.4	5.275	$5.265 \pm 0.020$	Si IV, C IV	$5.143 \pm 0.015$	5.214
SDSS J162629.19+285857.5	5.022	$5.035 \pm 0.010$	Si IV, C IV	$4.994 \pm 0.014$	5.023
SDSS J163411.82+215325.0	4.529	$4.587 \pm 0.010$	Si IV, C IV	$4.508 \pm 0.013$	4.501
SDSS J163636.93+315717.1	4.559	$4.590 \pm 0.020$	Si IV, C IV	$4.559 \pm 0.013$	4.570
SDSS J165902.12+270935.1	5.312	$5.316 \pm 0.005$	Si IV, C IV	$5.289 \pm 0.015$	5.306
SDSS J173744.87+582829.6	4.916	$4.905 \pm 0.020$	Si IV, C IV	$4.811 \pm 0.014$	4.919
SDSS J205724.14–003018.7	4.663	$4.686 \pm 0.005$	Si IV, C IV	$4.697 \pm 0.014$	4.685
SDSS J214725.71–083834.6	4.588	$4.597 \pm 0.005$	Si IV, C IV	$4.550 \pm 0.013$	4.583
SDSS J220008.66+001744.9	4.817	$4.782 \pm 0.010$	Si IV, C IV	$4.781 \pm 0.014$	4.799
SDSS J222509.19–001406.9	4.885	$4.882 \pm 0.010$	Si IV, C IV	$4.837 \pm 0.014$	4.883
SDSS J222845.14–075755.3	5.142	$5.150 \pm 0.010$	Si IV, C IV	$5.132 \pm 0.015$	5.143
SDSS J225246.43+142525.8	4.904	$4.881 \pm 0.010$	Si IV, C IV	$5.000 \pm 0.014$	4.905
SDSS J234003.51+140257.1	4.559	$4.548 \pm 0.010$	Si IV, C IV	$4.531 \pm 0.013$	4.551



**Figure A1.** Gemini/GMOS spectra of the 163  $z_{\text{em}} > 4.4$  quasars obtained in the GGG survey. The blue lines indicate the data obtained with the B600 grating at a spectral resolution  $\text{FWHM} \approx 5.5 \text{ \AA}$ . The red lines, which overlap the blue data near Ly  $\alpha$ , trace the R400 grating observations ( $\text{FWHM} \approx 8.0 \text{ \AA}$ ). CCD gaps give the zero values in these red spectra. All spectra were fluxed using several spectrophotometric standard stars and scaled to the available SDSS spectra. The R400 spectra taken with GMOS-S show fringing residuals at  $\lambda \gtrsim 8300 \text{ \AA}$ , leading to enhanced sky line contamination.

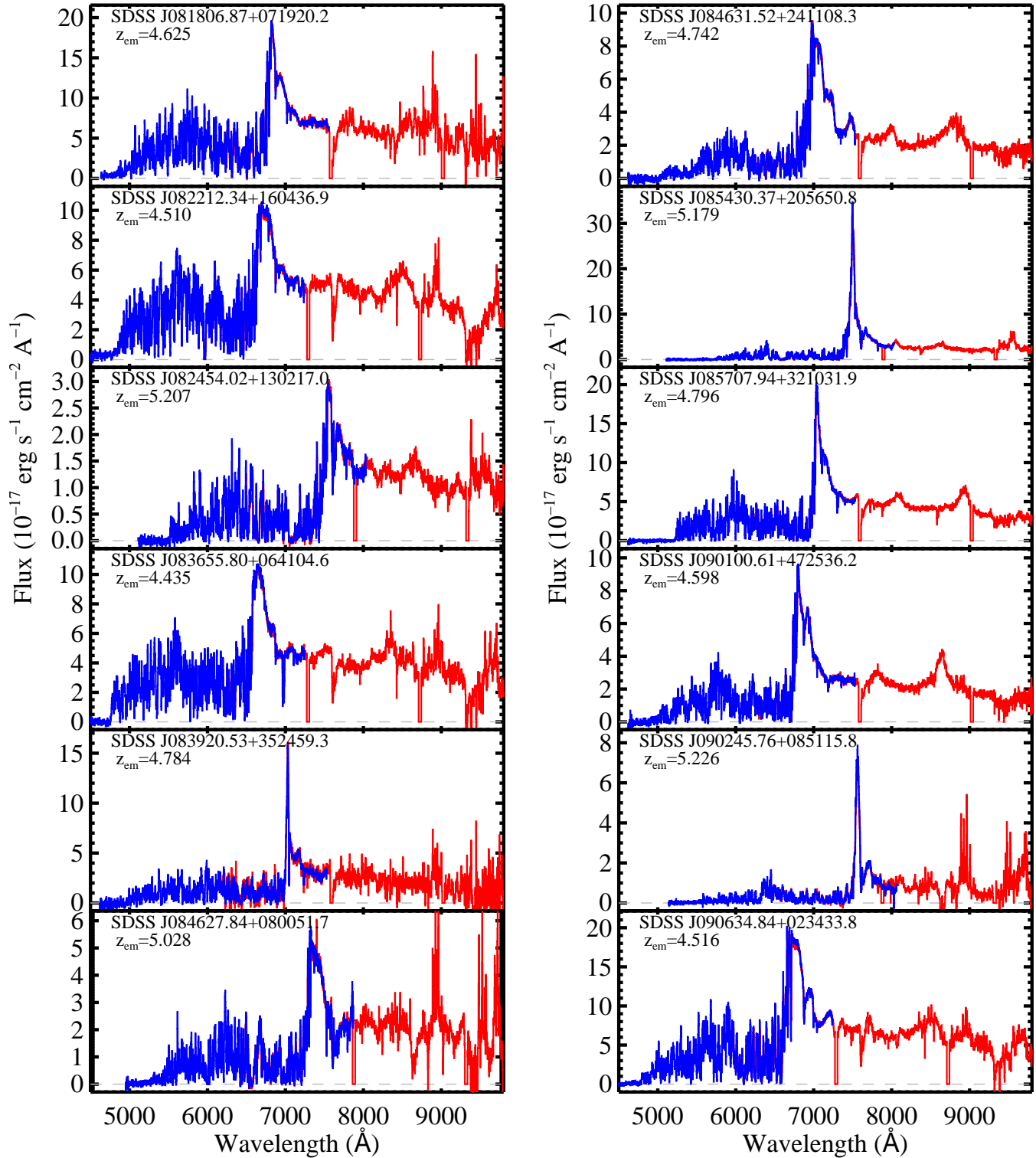


Figure A1 – continued

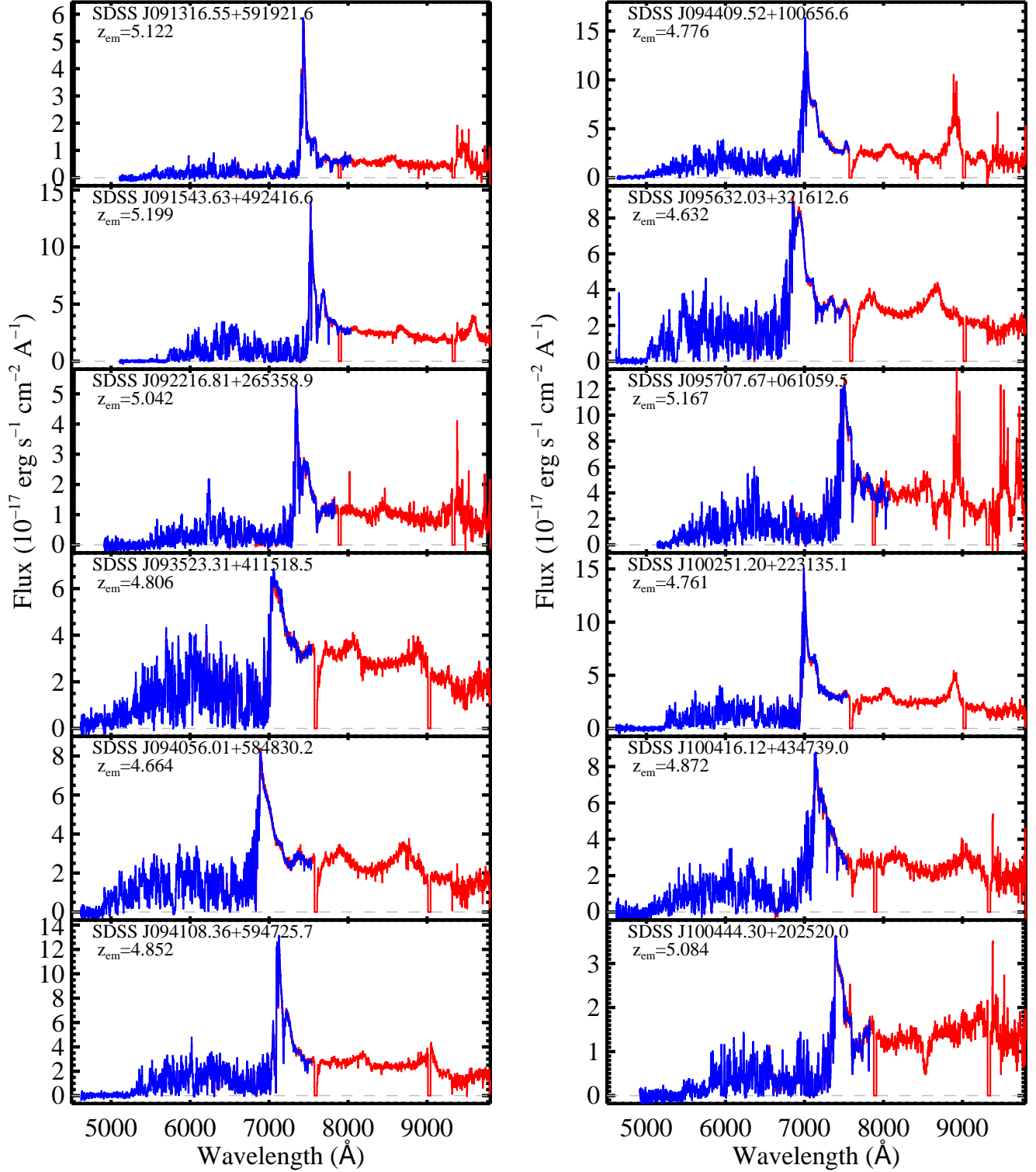


Figure A1 – continued

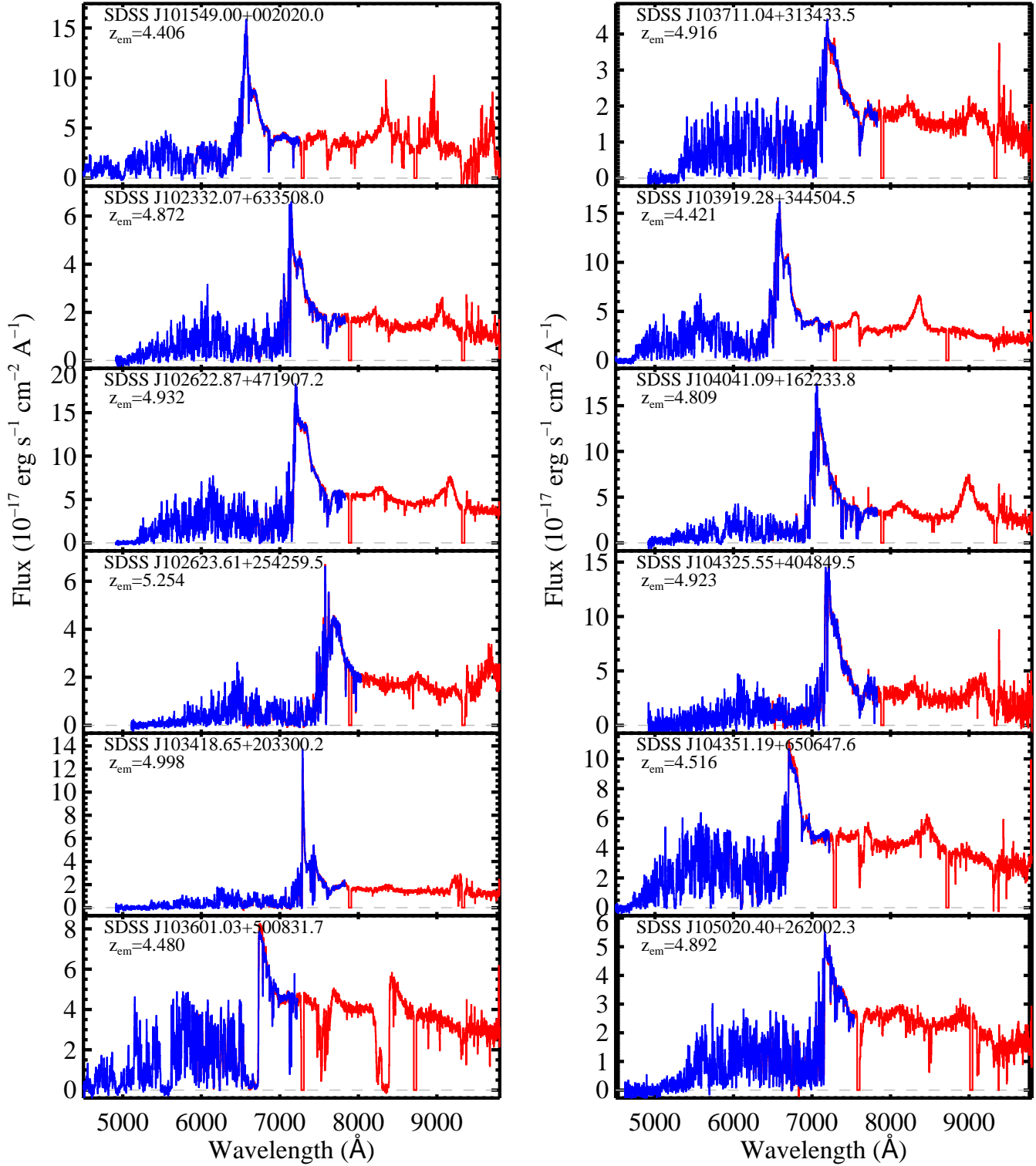


Figure A1 – continued



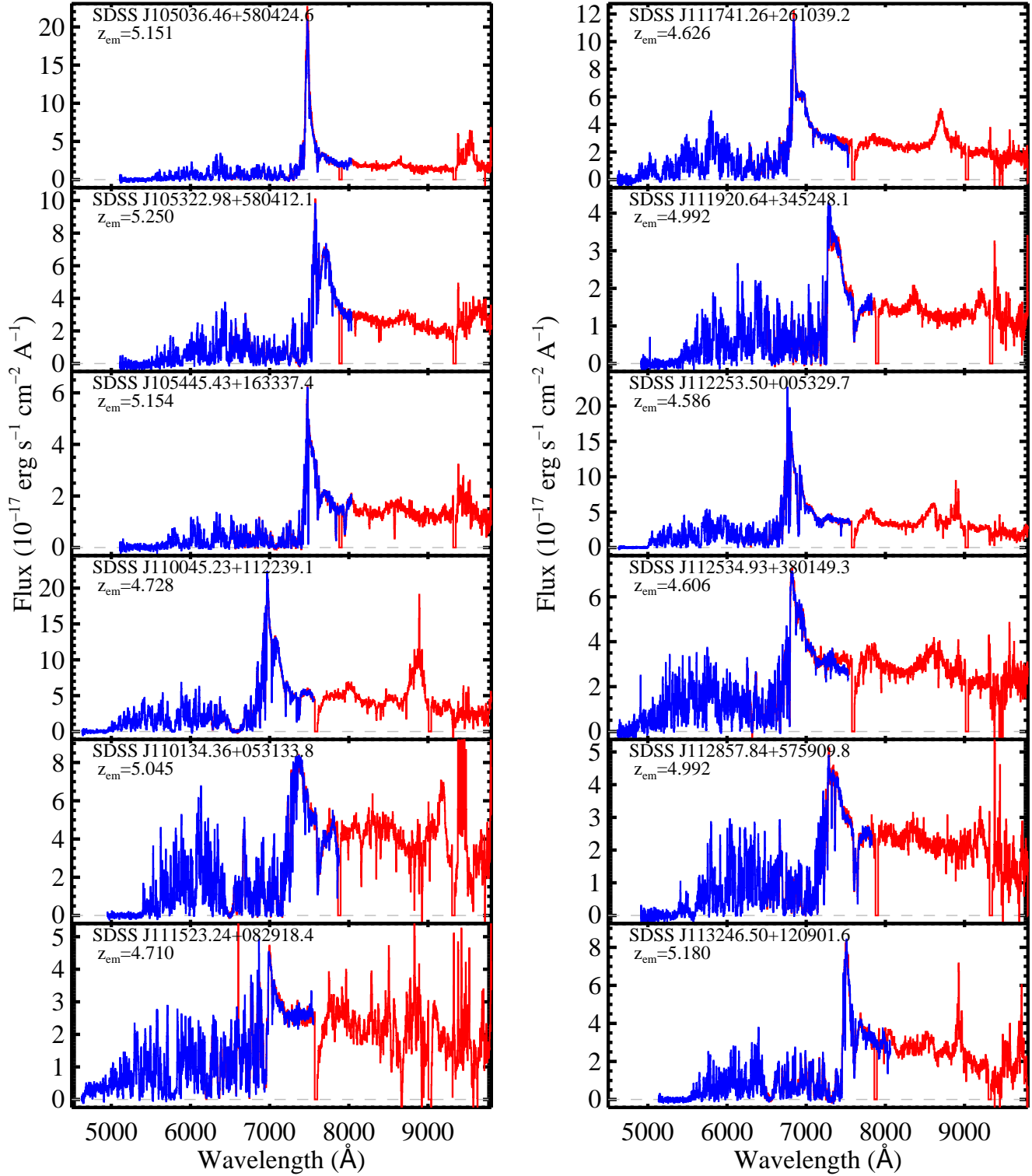


Figure A1 – continued

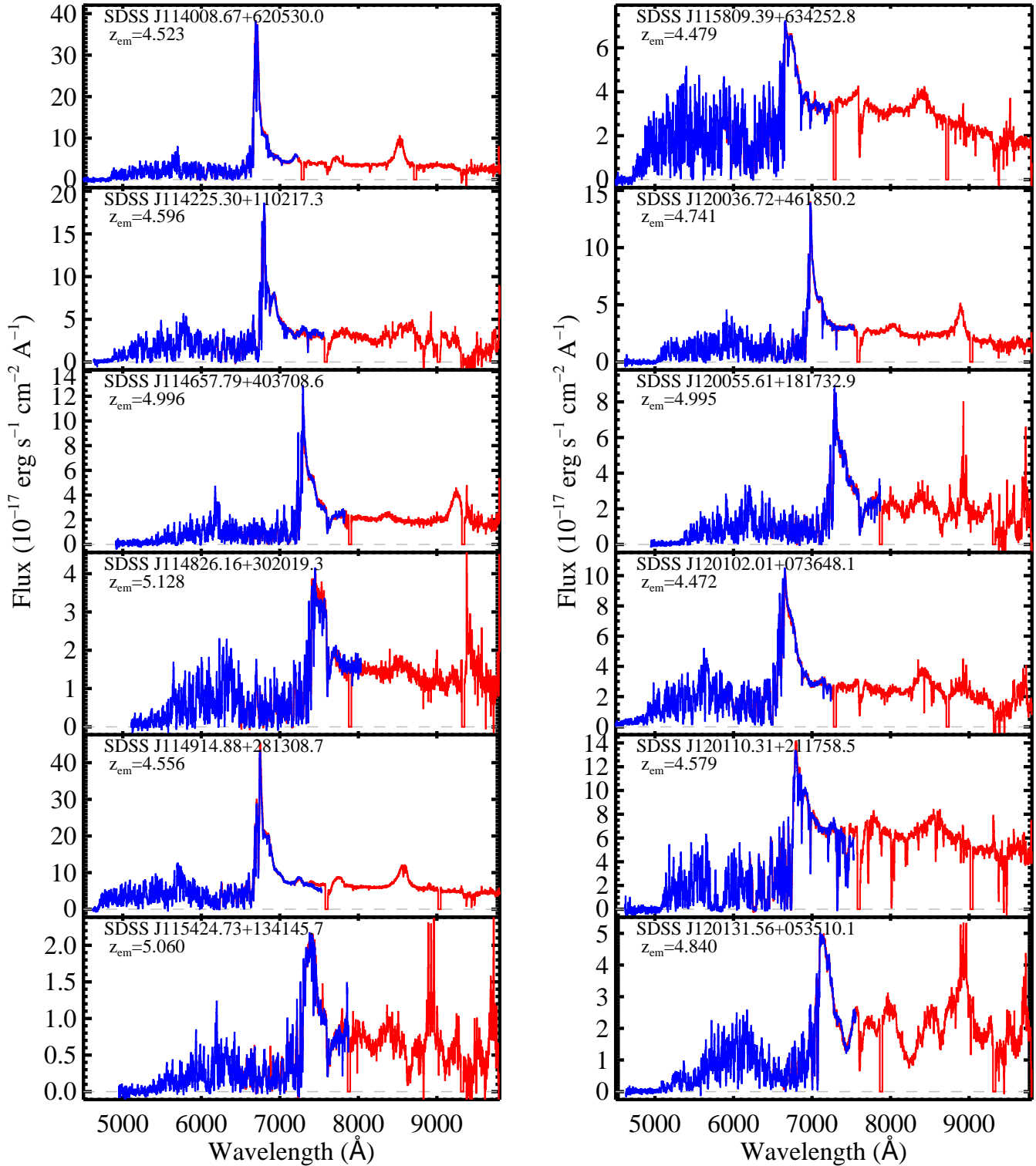


Figure A1 – continued

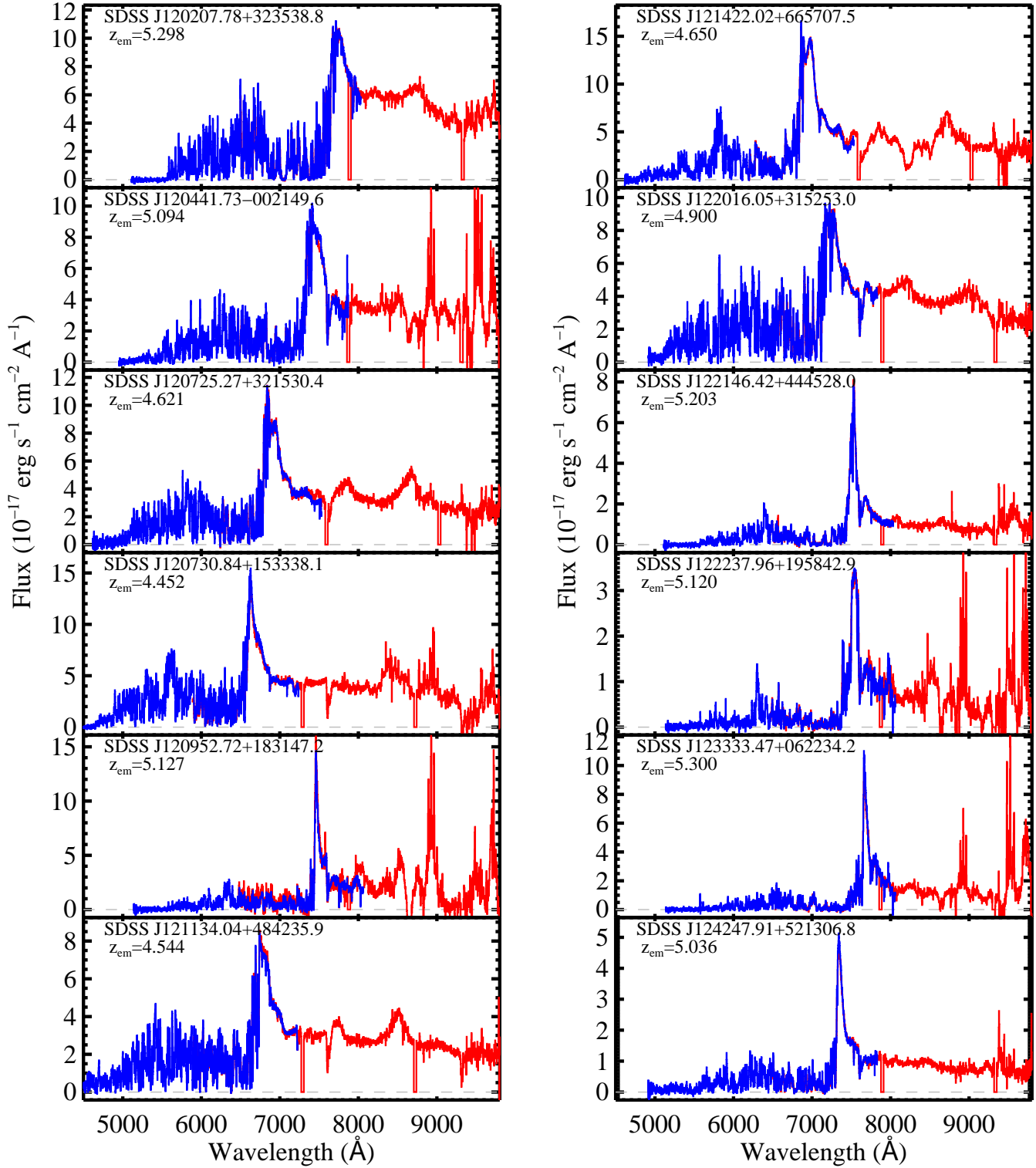


Figure A1 – continued

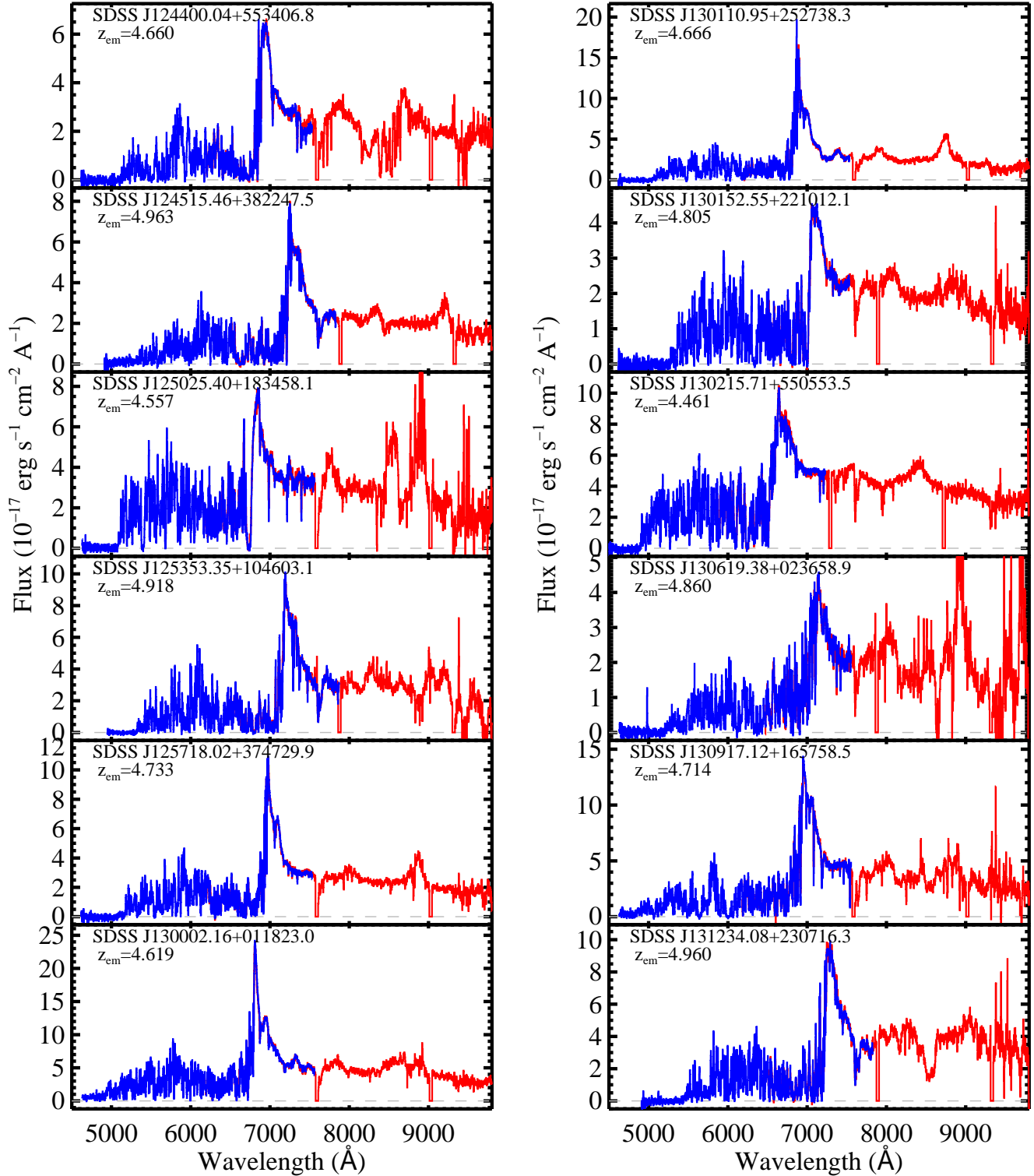


Figure A1 – continued

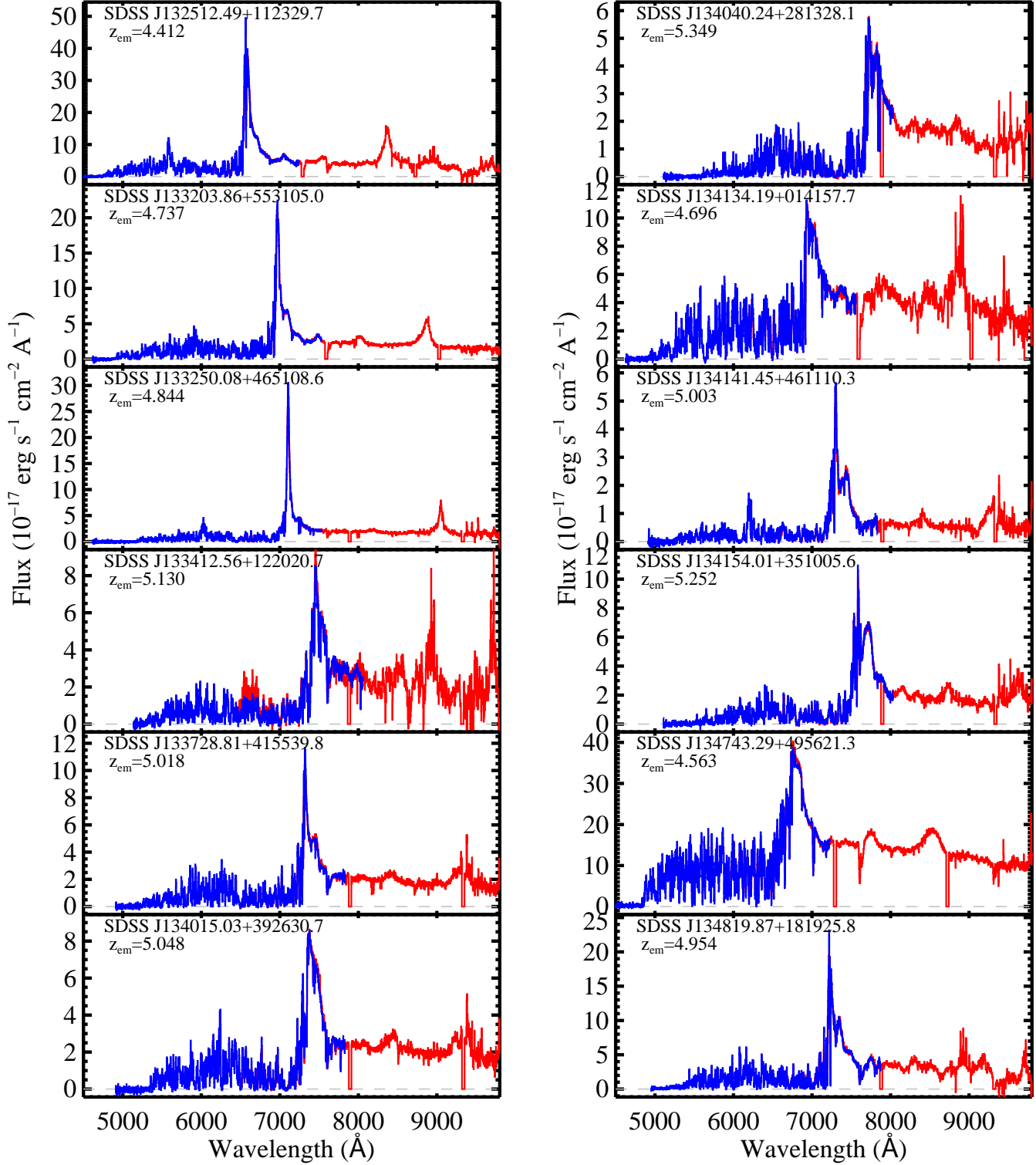


Figure A1 – continued

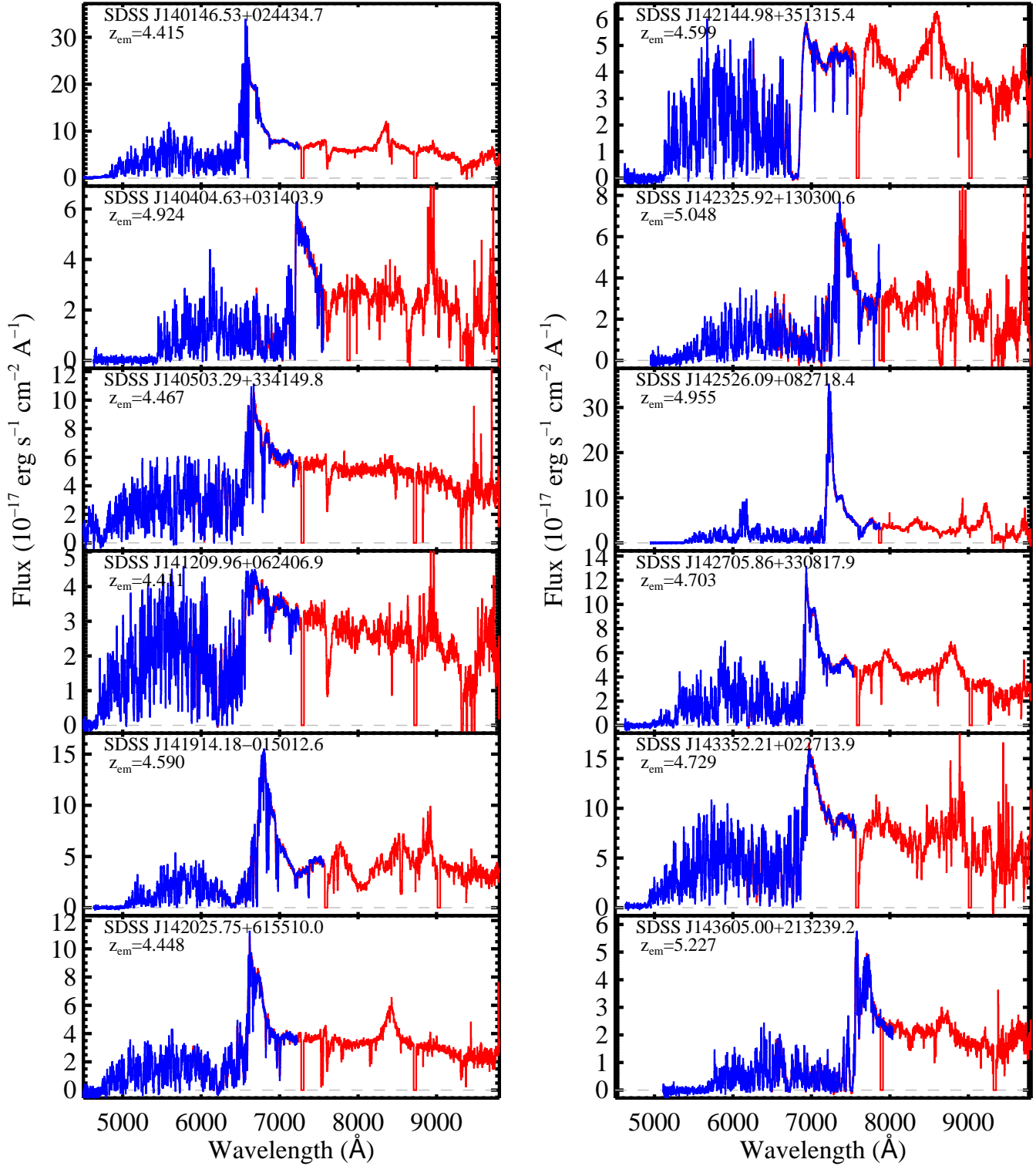


Figure A1 – continued

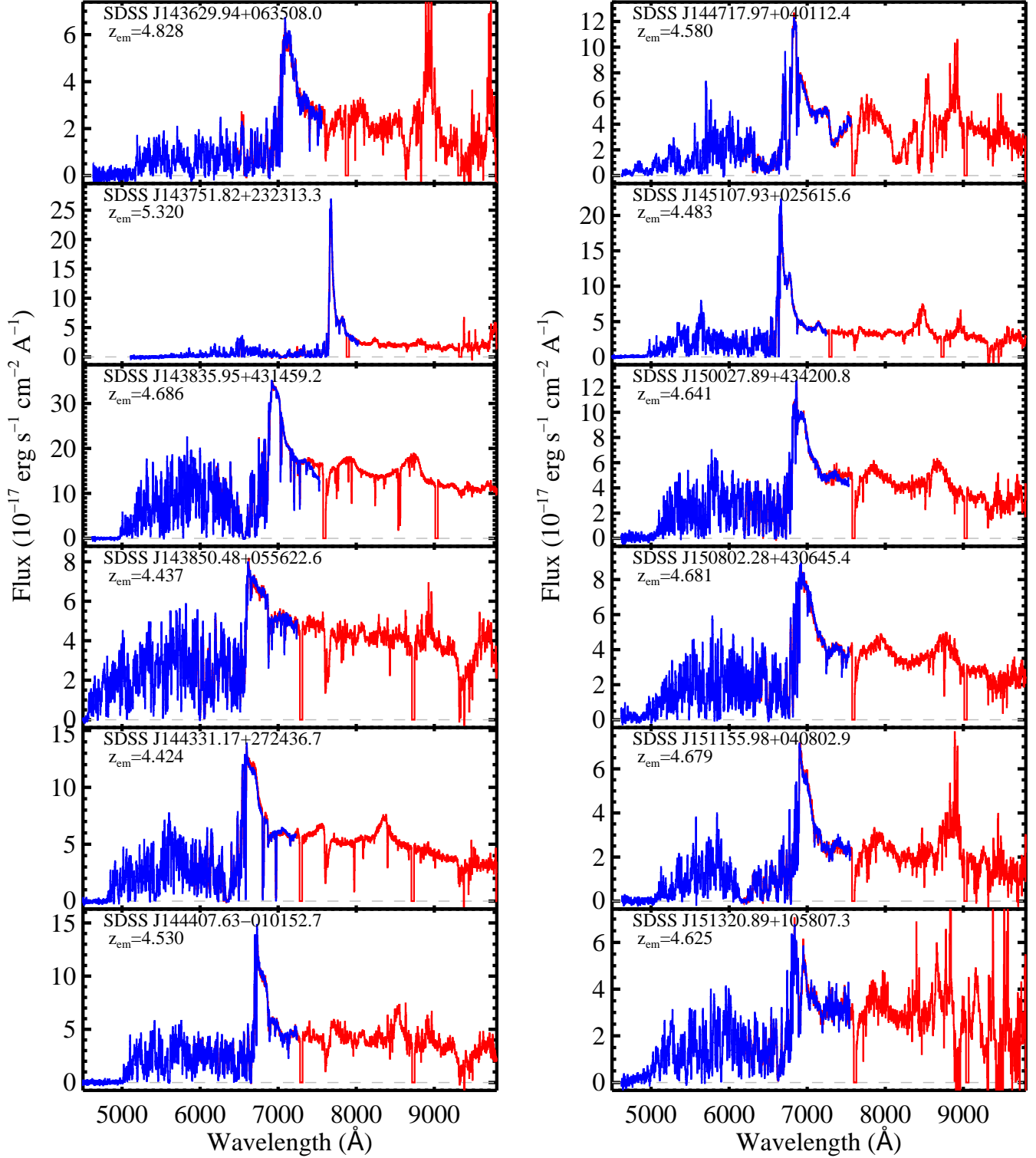


Figure A1 – continued

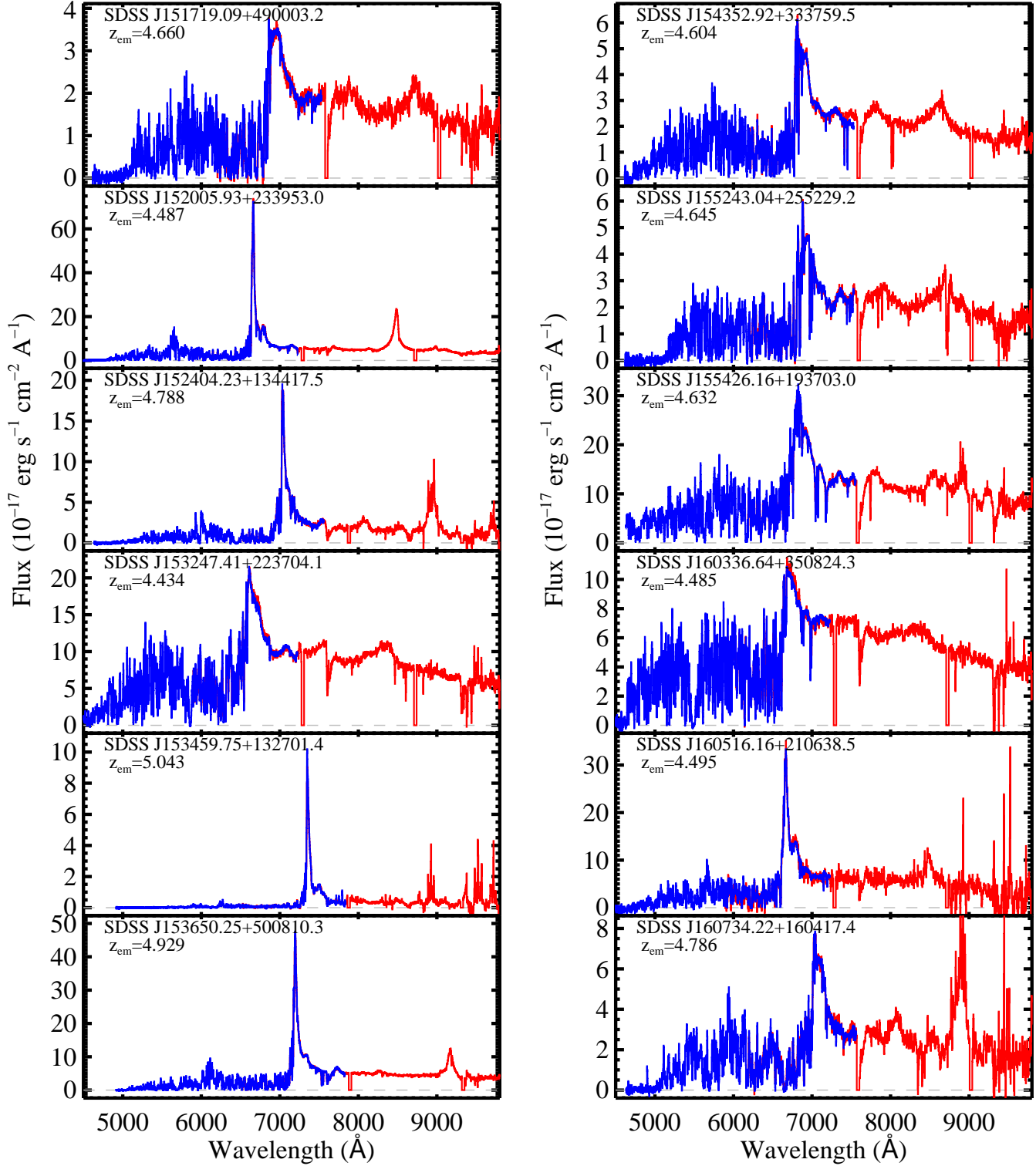


Figure A1 – continued



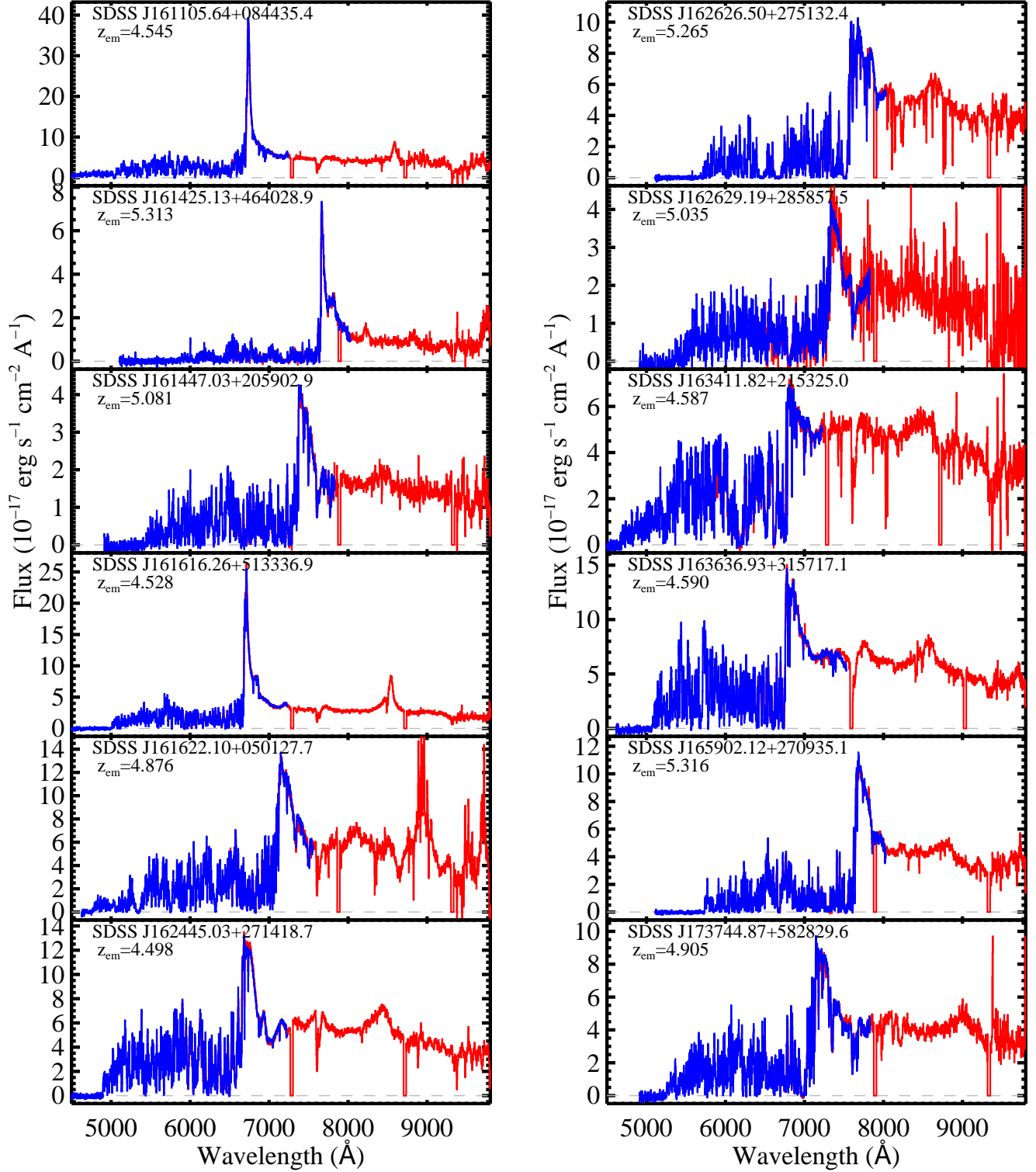


Figure A1 – continued

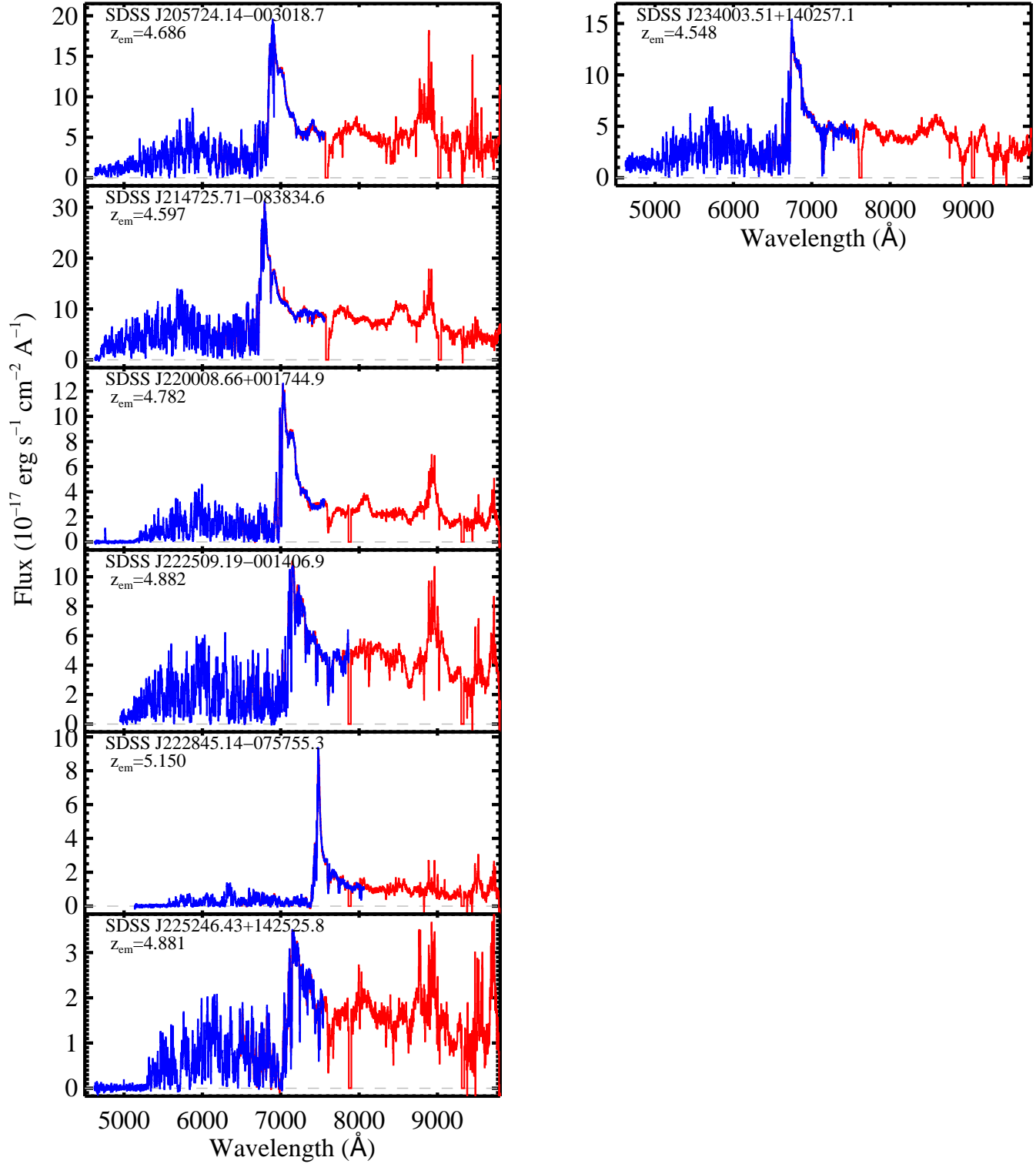


Figure A1 – continued